EFFECT OF WATER CONTENT IN ETHANOL ON SPRAY FORMATION AT SUBCOOLED AND FLASH-BOILING CONDITIONS

P.G. Aleiferis*
Department of Mechanical Engineering, Imperial College London, UK

J. Shukla
Department of Mechanical Engineering, University College London, UK

M. Brewer
Shell Global Solutions International BV, Amsterdam, NL

R.F. Cracknell
Shell Global Solutions (UK) Ltd., London, UK

*Author for Correspondence:
Prof. Pavlos Aleiferis
Imperial College London
Department of Mechanical Engineering
Exhibition Road, London SW7 2AZ, UK
Tel: +44-(0)20-75947032
E-mail: p.aleiferis@imperial.ac.uk

Full length article accepted for publication in the International Journal of Heat and Mass Transfer.

ABSTRACT

Direct-injection spark-ignition engines can be more sensitive to fuel type as the time available for spray formation and mixing is rather limited. The challenge is further complicated by fuel stock which includes a significant bio-derived component in some markets to manage fuel sustainability. The thermophysical properties of bio-components like ethanol differ markedly from typical hydrocarbons found in gasoline like *iso*-octane. Moreover, the production of anhydrous ethanol fuel involves separating water and ethanol by distillation and dehydration in an energy intensive process. This study presents results from an optical investigation into the spray formation process of hydrous ethanol fuels with 4–15% water content per volume in direct comparison to anhydrous ethanol and *iso*-octane. Injection tests were carried out with 20–110 °C fuel temperature at 1.0 bar and 0.5 bar gas pressure to mimic thermodynamic conditions of cold-start and fully-warm engine at low-load and wide-open-throttle operation. High-speed spray imaging was conducted along with droplet sizing by phase Doppler anemometry. The thermophysical properties of all fuels, including vapour pressure, density, viscosity and surface tension, as well as distillation curves, were obtained over a range of temperatures and the respective Reynolds, Weber and Ohnesorge numbers were considered in the analysis. At 20 °C *iso*-octane and anhydrous ethanol exhibited similar spray plume penetration, whilst increasing water content in ethanol reduced spray penetration. At higher temperatures up to 90 °C, anhydrous ethanol showed lower penetration than *iso*-octane whilst the hydrous fuels still exhibited lower penetration than anhydrous ethanol in sequence of increasing water content. At 110 °C, the ethanol fuels showed signs of plume merging and spray collapse, particularly at 0.5 bar gas pressure, with clear differences from *iso*-octane. The degree of plume merging and collapse was stronger with increased water content. The cone angle for the hydrous fuels was higher than that of pure ethanol, with the 4% water content ethanol that was close to the azeotropic point showing wider cone angle at temperatures higher than 20 °C, being distinctly higher at 90 °C. *Iso*-octane had consistently smaller droplet Sauter mean diameter than the ethanol fuels. As the percentage of water content in ethanol increased there was an increase in droplet sizes at all conditions.

INTRODUCTION

ALTERNATIVE FUELS FOR SPARK-IGNITION ENGINES

Ethanol is the most consumed biofuel worldwide [1, 2]. It is used extensively as an alternative fuel for spark-ignition engines, although studies of dual fuel ethanol-Diesel combustion have also been performed [3]. Apart from benefits related to sustainability, high content ethanol-gasoline blends have also been associated with lower particulate number emissions in downsized engines [4]. Although the energy density of ethanol per volume is approximately 30% lower than that of gasoline this figure can be mitigated if the high latent heat of vaporisation and high octane number of ethanol are utilised to increase engine efficiency. However, with high ethanol content fuel blends certain issues may arise at cold-start engine conditions due to lack of fuel volatility [5]. Ethanol is also water soluble which necessitates rigorous procedures during fuel distribution. Ethanol fuel specifications worldwide traditionally dictate use of anhydrous ethanol. Anhydrous ethanol is the grade of ethanol that has been dehydrated to a minimum purity of 99.6% [6]. Hydrous ethanol is the grade of ethanol that can be produced by simple distillation, *i.e.* without the further dehydration steps necessary to produce anhydrous ethanol [7]. Separating water and ethanol by way of distillation is an energy intensive process, especially when levels of ethanol purity > 85% are sought. Therefore, the production process of ethanol fuel is constantly investigated to achieve as low carbon footprint as possible [8, 9]. Moreover, at the ethanol-water azeotropic point of 96.5/3.5 by volume no further separation can be achieved by simple distillation and additional energy must be provided to produce anhydrous ethanol by other costly methods like membrane-distillation, pressure swing distillation, entrainer-addition distillation, molecular sieve separation, *etc.* [10–12]. Therefore, the total amount of energy required to obtain anhydrous ethanol accounts for a significant percentage of anhydrous ethanol's heating value [13].

USE OF HYDROUS ETHANOL IN ENGINES

Addressing energy requirements for ethanol production and associated costs may involve using directly hydrous ethanol as an alternative fuel. In recent years, various studies have been undertaken to assess the viability of hydrous ethanol as a fuel for internal combustion engines. A range of blends have been tested from about 4% to 40% water content per volume. Hydrous ethanol leads to higher engine brake specific fuel consumption due to the lower heating value of hydrous ethanol. However, the high latent heat of ethanol and the presence of water in ethanol that enhances latent heat effects further, reduces air intake charge temperature, and offers higher volumetric efficiency and lower NO_X emissions, increases brake thermal efficiency and can decrease unburnt hydrocarbons and CO emissions under some operating conditions [14–18]. Studies have also been performed in optical engines where the decrease in flame speed has been quantified [19, 20]. In general 10–15% water content has been considered quite tolerable and with good life-cycle benefits, noting that optimizing engine design to leverage gains in octane number and charge cooling corresponding to water addition on fuel economy could offset the reduction in the fuel's heating value [21]. A combination of laminar burning velocity measurements in constant volume bombs and heat release engine data have suggested that even with 20–40% water content by volume in ethanol, combustion performance may still be acceptable if the ignition timing is advanced [22, 23]. However, there are various practical problems in using such high levels of water so it is noted that this is a hypothetical option rather than a practical one.

It is also noted that the vapour pressure of gasoline-ethanol blends can be much higher than the vapour pressure of either ethanol or gasoline because the blend deviates from the ideal solution behaviour (Raoult's law) and this alters significantly the fuel's distillation curve [24, 25]. Although the presence of water in ethanol may offer benefits due to additional charge cooling effects, it is well known that the low vapour pressure and poor atomisation of pure ethanol can lead to problematic cold-start engine operation. This when coupled to water presence in ethanol can worsen engine cold-start issues. Practically, ethanol-fuelled engines do not start at temperatures below ~12 °C, while gasoline-fuelled engines can start at temperatures of -30 °C or even lower. This is one of the reasons that fuel-flexible vehicles in some parts of the world are rated to using up to 85% ethanol content per volume in gasoline (E85) instead of 100% ethanol. Moreover, Direct-Injection Spark-Ignition (DISI) engines are quite sensitive to fuel type as the

window for injection timing is narrow; advanced timing can lead to piston wetting while retarded timing does not allow sufficient time for in-cylinder fuel evaporation and mixing with air. Therefore, there is a need for understanding the spray formation process of hydrous ethanol, particularly with systematic increase in water content, as there are no data readily available in the literature over a wide range of conditions from subcooled to superheated injection.

PRESENT CONTRIBUTION

Multi-hole injectors for DISI engines offer atomisation benefits and flexibility in fuel targeting by selection of the number and angle of the nozzle's holes. However, there are no studies of spray formation from multi-hole injectors with hydrous ethanol in direct comparison with anhydrous ethanol and typical hydrocarbon components of gasoline like *iso*-octane, particularly over a wide range of conditions. The aim of this work was to develop fundamental understanding of the effect of water content in ethanol in terms of atomisation and breakup. Tests were carried out in a quiescent injection chamber using optical diagnostics. Specific objectives are listed below:

- Observe by high-speed spray imaging differences in injection characteristics of anhydrous and hydrous ethanol over a practical range of water content and compare with *iso*-octane.
- Characterise spray development by quantifying plume penetration and cone angle at fuel temperatures ranging from subcooled to superheated injection.
- Measure droplet sizes to understand effect on water content on spray breakup and atomisation.

The study also aimed to obtain thermophysical properties for the fuels tested and examine respective Reynolds, Weber and Ohnesorge numbers in connection to atomisation. Overall this work contributes to a database of spray formation measurements which are essential for developing our knowledge of the underlying mechanisms responsible for atomisation under realistic engine conditions. Such a database is also useful to spray modellers because accurate simulation of spray break-up mechanisms from first principles is very challenging, especially at conditions that common spray models have not been tuned to work automatically with. Models of flash-boiling atomisation that predict spray collapse for multi-hole injectors have recently been developed and new experimental data for their validation with a range of practical fuel types are highly sought after [26–28].

EXPERIMENTAL APPARATUS AND PROCEDURE

INJECTOR

A multi-hole injector designed for vertical installation in close spacing arrangement with the spark plug of a DISI engine was used. The injector was a prototype and had six nozzle holes (in 3 plume pairs) in an asymmetric arrangement with different angles in respect to the vertical axis. A schematic of the injector is shown in **Figure 1**. All injector holes had ~0.2 mm internal diameter with an outer counterbore of ~0.5 mm in diameter. The length to diameter ratio for the inner hole was about 2 and for the outer hole about 1. The nozzle holes of this generation of injector have been characterised by silicon castings and microscopy, with results for the production version of this injector (with slightly different counterbore diameter and inner length) that can be found in [29, 30]. Fuel pressure was set at 160 bar. The injector has been used with many different fuels over a wide range of fuel temperatures from 20 °C to 180 °C and air pressures from 0.3 bar to 5 bar in constant volume injection chambers [31–33] and in an optical engine [34–38]. The injector flow rate can be found in [29, 30], with modelled sprays at the respective flow rate found in [39–41]. Studies of the injector/driver delays have been presented in [32], whilst a range of further details on injector delays and injector flow rate variations for the same generation of hardware can be found in [42].

INJECTION CHAMBER

All fuel injection events were conducted in two quiescent pressure chambers, one cylindrical and one octagonal sharing injector mounting and instrumentation. The chambers have been presented in detail in previous publications and not repeated here for brevity [31–33]. They enable simultaneous multi-technique characterisation such as imaging with back lighting or side lighting, and the use of on-axis and off-axis techniques for droplet sizing and velocity measurements (Phase Doppler Anemometry, PDA). The gas pressure (*i.e.* the injector's 'back' pressure) was monitored by an absolute pressure sensor. A valve at the bottom of the pressure chamber enabled evacuation of

liquid and vapour fuel, as well as creating sub-atmospheric pressure within the chamber, through connection to a large vacuum pump. The injector was fitted into a specially designed mount positioned at the centre of a crucible in the upper lid of the pressure chamber. A thermocouple was installed inside the injector's mount close to the injector tip. A band heater was attached to the injector to heat up its body temperature, replicating *in-situ* heating of injectors mounted in DISI engine heads. The thermocouple provided feedback to a controller which regulated the injector temperature as required for each test case. The term injector-body temperature in the current paper corresponds to the temperature reading of this thermocouple and it is considered to be that of the fuel temperature inside the nozzle of the injector given enough 'soaking' time.

TEST CONDITIONS

The fuel temperature was altered by the heating the injector body as previously described to replicate engine running conditions. Specifically the injector was heated to 20, 50, 90 °C to represent typical ambient to fully warm engine operation. A further test temperature of 110 °C was included to replicate a heat sink scenario. To mimic engine in-cylinder pressure conditions for different direct injection strategies, 1.0 bar and 0.5 bar gas pressures were employed (at 20 °C) to simulate early homogeneous injection strategies for part-load and wide open throttle engine operation.

Table 1. Varied Test Conditions.

Fuel Temperature [°C]	Chamber Pressure [bar]
20	0.5, 1.0
50	0.5, 1.0
90	0.5, 1.0
110	0.5, 1.0

SPRAY VISUALISATION SETUP

The injector was mounted at 19° to the vertical in order to optimise the imaging arrangement. The spray was recorded at a frame rate of 9,000 frames per second, equivalent to one spray image at each Crank Angle degree (°CA) for an engine running at 1500 RPM. The camera allowed a maximum spatial resolution of 640×480 pixels at this frame rate (160 μm/pixel). The shutter was set to 1 μs. Illumination was achieved with backlighting using a Multiblitz Variolite 500 photographic spark flash of 4 ms duration diffused through a semi opaque Perspex sheet. The image was a shadowgraph of the spray, therefore only the liquid phase was visualised with this technique. As a result of the back illumination method and the geometry of the injector, each imaged spray plume was the superposition of two plumes (see *z-y* view in **Figure 1**). Triggering of the high speed camera, flash lamp and solenoid valve was provided by an AVL 327 engine timing unit. Injection duration was held constant at 1.5 ms pulse width for all conditions, with the camera recording for 2.5 ms each injection to capture initial, steady-state, end of injection and post injection spray characteristics. Due to obscuration of the spray tips by the pressure chamber windows, it was only possible to measure spray tip penetrations until approximately 1.2–1.4 ms After the Start Of Injection (ASOI, *i.e.* the time period following the rising edge of the trigger pulse sent to the injector driver unit). The average driver delay from the start of the injection pulse (Start of Injection, SOI) to fuel seen at the injector tip was of the order 300 μs, as has been quantified in detail in [33]. 100 injection events and an average background image were captured at each timing ASOI. The background image for each time interval in the imaging sequence was removed from the spray images. Each corrected image was then thresholded to leave a binary image. The image was then rotated to align each plume pair with the vertical axis and each plume pair was 'scanned' to find the plume tip. The distance from the plume tip to the nozzle was scaled to calculate plume length. To determine the optimum threshold for automated processing, detailed sensitivity analysis was carried out on the penetration based on different threshold levels using considerable in-house expertise and the uncertainty in the calculated values was found to be better than 1–2% over the duration of injection. The process included noise filtering and adaptive thresholding, with emphasis on image sub-windows

around the plume tip. The outer envelope cone angle of the spray was calculated between 2 mm and 12 mm distance from the injector nozzle. Apart from side imaging of the plumes, a 45° mirror was installed to obtain a 'footprint' base view of the spray where all 6 plumes could be seen simultaneously. Side illumination was used in this case and Mie scattering spray images were recorded.

DROPLET SIZING

Droplet sizing of the spray was carried out using a TSI Phase Doppler Anemometry system. The Phase Doppler technique is well established and details on its principles and uncertainties can be found in [41]. The system consisting of a Coherent Innova 70C Argon-Ion laser (5 W) coupled to a TSI beam splitter and Bragg cell. Both the transmitter and receiver had an optical focal length of 250 mm. To focus on breakup without effects from plume interactions, and to achieve adequate optical transparency through the spray for measurements to be taken, one of the plumes, plume 5 in **Figure 1,** was isolated using a specially made metal plate with a v-shaped cut to allow the spray of plume 5 through into the optical access field. The rest of the plumes were diverted by the plate and funnelled out away from the optical access field. The plate was fixed in place and restrained securely to restrict movement. Images of the isolated spray plume were acquired with a high-speed camera to ensure that the isolation plate did not move and the nozzle's other plumes did not interact with the isolated plume, *i.e.* that the fuel coming out of the remaining holes was simply directed out of view. The injector was orientated so the system's measurement volume traversed along a straight horizontal line from the inner edge (closest to the injector body axis), through the spray centre and to the opposite outer spray edge (closest to the cylinder bore in a real engine) of the isolated spray plume. Droplet measurements were conducted at the centre of the plume 25 mm vertically down from the injector tip. Droplet sizes and 2-component velocity data were acquired for 200 injections in each case, leading to approximately 10,000–20,000 valid droplet data counts at each measurement location depending on the optical density of the spray. It is also noted that PDA data quality can be significantly affected by various system settings and so detailed tests were carried out initially using considerable in-house expertise in order to identify the most appropriate set of parameters for this measurement campaign. The effect of temperature dependence of the refractive index of the fuels was considered on the basis of previously published work in this area [30, 33, 43–46]. The injection chamber was purged for 2 s after each injection event and time was allowed for settling of any residual airflow before the next injection. To save time and to achieve measurement consistency an in-house programmed control system, interfaced with the AVL 427 engine timing unit was used to synchronise the injection, PDA data acquisition trigger, and purging events.

FUELS

Several fuels were investigated: Anhydrous ethanol (E100), hydrous ethanol with 4%, 6%, 10%, 15% water content per volume (named E96W4, E94W6, E90W10, E85W15, respectively) and *iso*-octane. *Iso*-octane is a single mid-distillation component of gasoline with boiling point almost the same to water's at atmospheric pressure. It was selected because it is commonly used as substitute for gasoline in engine research applications due to its single component nature. However, it is noted that higher volatility components like pentane are better substitutes for gasoline in the context of mimicking spray collapse at superheated fuel conditions [31, 33]. It is also noted that apart from its relevance as a hydrous ethanol component, there has been great interest recently in the atomisation of water by direct injection for increasing the thermal efficiency of engines [47–51]. Some typical thermophysical properties related to atomisation and phase change are summarised in **Table 1** at atmospheric temperature and pressure for easy reference.

The dependence of properties on temperature was considered by obtaining correlations from [49, 50] for *iso*-octane and water. For anhydrous and hydrous ethanol, density, viscosity and vapour pressure were provided by Shell over a range of temperatures from 10–60 °C. Then a best fit approximation was applied to estimate values at lower and higher temperatures than those measured. The extended range for anhydrous ethanol was found to fit well with ethanol data obtained from [52, 53]. The respective properties for hydrous ethanol were compared with data available in [54–56] and a good match was also observed. Values of surface tension for anhydrous and hydrous ethanol were

provided by Shell at 20 °C. The dependence of surface tension on temperature was obtained by correlations from [52, 53]. Values were compared with data from [55] and a good match was again observed.

The distillation curves of the two alcohols were provided by Shell and shown in **Figure 2**. Anhydrous ethanol exhibits a boiling point of ~77.1 °C which is lower that the nominal boiling point of pure ethanol that is ~78.4 °C. The difference is attributed to 'denaturing' agents added to ethanol to make it unsuitable for drinking.

Table 1. Selected Properties.

Properties	*iso*-Octane	Ethanol	E90W10	Water
Density [kg/m^3]	692	794	824	998
Viscosity [cP]	0.5	1.2	1.7	1.0
Surface Tension [mN/m]	14.7	22.4	26.3	72.0
Latent Heat [MJ/kg]	0.305	0.902	1.10	2.440
Heat Capacity [kJ/kgK]	1.15	2.46	2.68	4.18
Energy Density [MJ/kg]	45	29	25	–
Boiling Point [°C]	99.2	78.4	Distillation	100
Vapour Pressure [kPa]	5.2	5.9	4.8	2.3

The vapour pressure curves of the fuels are shown in **Figure 3**. Hydrous ethanol shows small differences from anhydrous ethanol over the scale of temperatures shown. **Figure 4** shows the density of the fuels tested. *Iso*-octane is the least dense out of all the fuels. As the water content in ethanol was increased the density also increased as expected. **Figure 5** shows the dependence of kinematic viscosity on temperature. It is noted that initially as water content is increased the kinematic viscosity of the hydrous fuel doesn't lie between anhydrous ethanol and water but instead it increases to levels higher than pure ethanol's. This is gradual as water content increases to 4%, 6%, 10%, 15%. This effect was examined against data from [54–56] and this behaviour was confirmed. This behaviour persists till levels of water content of about 50–60 % per volume and then the kinematic viscosity starts to decrease towards the kinematic viscosity of pure water. This non-linear behaviour leads to E90W10 having the same kinematic viscosity as a hydrous ethanol fuel of about 70% water content at 293 K. At higher temperatures the dependence of kinematic viscosity of hydrous ethanol on water content become flatter, leading to the kinematic viscosity of E90W10 being similar to about 60% water content per volume at 323 K according to [55]. **Figure 6** shows the dependence of surface tension on temperature. As water content is increased the surface tension of hydrous ethanol lies between anhydrous ethanol E100 and water, hence hydrous ethanol is expected to atomise less efficiently than E100. This behaviour can also be observed for a wider range of water content in [55]. The combination of higher surface tension at increasing water content along with the higher kinematic viscosity of the hydrous blend (despite the lower kinematic viscosity of water in comparison to that of anhydrous ethanol) points to further negative effects on atomisation.

Non-dimensional numbers were calculated on the basis of the nozzle hole's diameter of 0.2 mm and a velocity of the order 100 m/s as calculated from the mass flow rate of the injector. **Figure 7** shows the Reynolds number *vs.* temperature. It is clear that E85W15 has the lowest Reynolds number of the hydrous ethanol fuels tested here, reaching nominal values close to laminar conditions at the coldest temperatures. The liquid Weber number in **Figure 8** follows the same pattern as the Reynolds number with E85W15 displaying the lowest values of all fuels. The differences between the hydrous and anhydrous ethanol suggests that anhydrous ethanol is more likely to atomise more readily than its hydrous counterpart. It is also noted that water exhibits clearly much lower values than all the fuels shown, highlighting the difficulty in atomising water from the same injector at the same conditions. The Ohnesorge number was plotted at each temperature by using the respective values of Reynolds and Weber in **Figure 9** and was also used to plot the classic Ohnesorge diagram [57] in **Figure 10**. The latter combines the viscous, inertial

and surface tension effects to determine which regime the fuel sprays fit into according to [58]. It is noted that as Reynolds numbers move to the left, one can see the effect of sub-zero temperatures where the alcohols move away from the atomisation regime and into the second wind induced regime. Water approaches the border between regimes already at temperatures close to 0 °C. For analysis of sprays at sub-zero fuel temperatures the interested reader may refer to [59].

RESULTS

GENERAL SPRAY CHARACTERISTICS

Sprays from individual injection events at 20 °C, 1.0 bar are shown in **Figure 11** for the side view with *iso*-octane, E100, E90W10 and E85W15. Spray plumes typically became observable between 333–444 µs ASOI depending on fuel type and conditions. In most cases, the spray development could be described as a three-stage process. The first stage covered the first 555 µs ASOI as the spray plume formed upon entry into the chamber while the flow configuration was still being developed inside the nozzle. The second was typically a quasi-steady-state from 666–999 µs ASOI, where the spray was unwavering with defined cone angles. Lastly, the spray between 1221–2109 µs ASOI could no longer retain its shape over the needle closure period and beyond, experiencing considerable distortion that started near the nozzle that set up large-scale oscillations in the liquid plume, particularly for the alcohols. The initial spray behaviour changed primarily based on whether the plumes had entered the chamber by 444 µs ASOI or 555 µs ASOI. If there were no plumes visible by 444 µs ASOI, the speed and penetration of 555 µs had the illusion of compensating by penetrating further, but by 777 µs ASOI the delay in entry would be balanced and typically similar to the earlier frame injection events.

The behaviour of plume pair A was different to that of plumes B and C (see **Figure 1** for reference). It seems that the steeper angle of the nozzle holes for this pair caused the plumes to retain a flatter and wider tip than plumes B and C. This was true for all fuels at 20 °C shown here, but also at 50 °C, both at 1.0 and 0.5 bar. From this view plume pair C seems to have displayed a slight dissimilarity in angle of penetration between the two superimposed plumes for all fuels, which gave the effect that the plume ‘split’. However, it is difficult to clearly identify or differentiate between the two superimposed plumes. This is particularly evident at 999 µs ASOI in **Figure 11** and likely a combination of in-nozzle cavitation and viscosity effects coupled to large-scale hydrodynamic ‘flapping’ of the plumes out of the nozzle, manifested by out-of-phase spray motion when comparing the two plumes of the pair. It is noted that in-nozzle cavitation has been confirmed by previous real-size optical nozzle work by the current authors [60, 61].

During the quasi-steady state phase of the spray’s development, there are indications of a slight formation of a vortex structure on the outer boundaries of plumes A and C from aerodynamic forces on the droplets. As the spray continues to 1221 µs ASOI it is possible to see the effect of hydrodynamic flapping from shear forces creating amplified unstable surface waves on the spray surface. This is likely also linked to flow separation locations inside the nozzle, and the formation of unstable recirculation zones causing the plumes to change their initial trajectory. Plume pair B for the ethanol fuels swings to the right while plume pair C converges towards the centre as a result of these effects. During the final two frames for the fuels in **Figure 11** the aerodynamic drag which could primarily be seen to have an effect on the tips of the plume can now be observed all the way along the plume to its nozzle exit point. The plumes have become much wider and the droplets between plumes B and C have a higher degree of interaction. By 2109 µs ASOI all plumes have crossed the illuminated area of the window.

Overall, very few differences can be spotted at ambient conditions between the fuel’s spray breakup when adding water to ethanol on a macroscopic scale. Close inspection highlighted that plume pair B after 1221 µs ASOI reduced in thickness as the percentage of water was increased. Narrower plumes are an indication of a reduction in the degree of atomisation. Since the surface tension of water at 20 °C is almost 3 times larger than ethanol’s, even a small percentage volume of water addition to ethanol leads to an increase in surface tension further affecting liquid jet breakup. It is also noted that the viscosity of hydrous ethanol for the water content shown is larger than both

anhydrous ethanol's and water's, affecting in-nozzle turbulence dampening (Reynolds number effects) and near-nozzle atomisation (Ohnesorge number effects).

Figures 12–13 display spray development events with *iso*-octane, E100, E90W10 and E85W15 fuels at superheated conditions of 110 °C at 0.5 bar and 1.0 bar, respectively. Onset of spray 'collapse' conditions is shown in **Figure 12** through the convergence between plumes B and C into a single plume formation. Plume pair A also exhibits slight contraction towards the central axis. The fuel has been quickly depressurised below its saturation vapour pressure from inside the nozzle holes due to cavitation effects and exits the holes widening in near-nozzle plume angle due to sudden increase in the droplets' radial momentum from enhanced breakup effects. The cone angle contracts downstream as the plumes are 'sucked' towards the centre of the chamber from low pressure effects. *Iso*-octane retains its spray plume orientation much better than the alcohols, especially when compared with the higher water content hydrous fuels. The visibility of these phenomena is more apparent when decreasing the pressure to 0.5 bar due to the reduction in the boiling point of all components further. The 'darkness' of the plumes increased as the injector body temperature was raised from 20 °C to 110 °C, more so as the gas chamber pressure was decreased, due to the higher degree of droplet density as fierce atomisation occurred. Close inspection shows how anhydrous ethanol retains its shape better than E90W10. The aerodynamic drag and frictional forces are more evident with the addition of water through the appearance of larger vortices from the shearing of the merged plume pair boundaries. The effect of these forces was observed to appear as early as 444 µs ASOI on the outer edges of plume pair A and C. Plume pair B exhibited more intense shearing alongside the left hand side, causing 'ripples' along the plume pair boundary with an appearance as if being 'peeled', particularly beyond 1110 µs ASOI. At 110 °C, 1.0 bar in **Figure 13**, separation can still be identified to a certain degree between plume pairs B and C for all fuels. At 1110 µs ASOI one can still see the 'second wave' of fuel spray formation. The tips are much more rounded at the higher temperature, more so at the lower pressure, as the superheated spray atomises intensely due to flash boiling effects.

Figures 14–15 show mean spray images, averaged over 100 injections (hence appear 'blurred'), at 777 µs ASOI from 20 °C to 110 °C at 0.5 bar and 1.0 bar gas pressure, respectively; these offer direct comparison of the mean behaviour of all fuels at a fixed timing. Penetrations and cone angles are quantified in detail in later sections but the reader may note qualitatively at this stage the lower penetration with higher water content and a small widening of the plumes at the lower gas chamber pressure along with an overall outer cone angle widening. A feature that appeared consistent for 20 °C and 50 °C for both pressures was the 'concave' structure at the tip of plume pair C. This feature gradually disappeared for some of the fuels at 90 °C and 110 °C. Lower percentages of water such as E96W4 and E94W6 exhibit a greater degree of discrepancy between the 'splitting' of the two plumes compared to the fuels with higher percentage of water. At the higher temperatures such splitting couldn't be observed for some fuels, especially *iso*-octane and anhydrous ethanol, as spray breakup was stronger and there was faster vaporisation at the tips. At 50 °C, the effect seems to be enhanced in comparison to 20 °C as the droplets possessed a higher velocity that caused a visual increase in the 'splitting' of the two superimposed plumes. The viscosity still has clear differences between the hydrous fuels at this temperature, which is not the case by 90 °C; the boiling point of ethanol has not been exceeded at 50 °C. Meanwhile, plume pair B had generally a narrower width than plume pairs A and C at 20 °C and 50 °C. At 90 °C *iso*-octane's spray still retains its nominal shape of three distinct plumes; the boiling point of *iso*-octane has not been surpassed. The sprays of all anhydrous and hydrous ethanol fuels exhibit initial convergence at 90 °C, associated with the onset of flash boiling effects. Plumes B and C interact with each other and begin to exhibit initial signs of 'mushrooming', where the spray starts to go back on itself and 'swells' in the upper region of the plume structure. Though, there is still clear partition between plume pairs B and C. The plume tips are more rounded at 90 °C which is an indication of higher degree of spray breakup.

At 110 °C, *iso*-octane retains still defined individual plumes but the tips are lighter in greyscale. There is a slight convergence of plumes B and C especially closer to the injector nozzle and the plume tips have become a lot more rounded due to increased vaporisation of droplets at the edges. Plume pair A shows a trend of reduction in plume

width for all ethanol fuels at both gas pressures, along with an increase in darkness due to denser concentration of droplets. At 110 °C, 1.0 bar, the spray formation is comparable to that of 90 °C, 0.5 bar. A consistent trend of rounder plume tips was found as the percentage of water was increased. Plumes B and C converge slightly more, still retaining a discernible separation. The addition of water didn't show any visible differences at this condition, other than the 're-merging' of the potentially split plume pair C and reduction in length as water percentage increased. At spray collapse conditions of 110 °C and 0.5 bar, the convergence of plume pair A towards B and C increases as the percentage of water increase and the effects of 'mushrooming' become more prominent. The effect of greater plume convergence with increased water content, along with respective signs of greater spray collapse, may be related to the higher heat capacity of water that could lead to hydrous ethanol fuels with greater water content retaining their temperature for longer.

All six plumes were analysed individually by using the base view of the spray. **Figures 16–17** show base view mean spray images at 777 µs ASOI at 0.5 bar and 1.0 bar gas pressure, respectively. These are complementing the side view's mean spray images of **Figures 14–15** and can help to understand if it is both plumes of every pair that are showing the same effects, or two plumes that are 'splitting'; therefore, the concave behaviour of the plume pairs seen from the side can be explained. When looking at E96W4, the lower central plume at 20 °C in **Figure 16** shows a flatter tip and a closer distance to the lower left plume compared with the pointier upper middle plume. Moreover, when taking a closer look at E90W10 at 50 °C in **Figure 16** for instance, the two left most plumes clearly have a difference in their penetration length. This can also be seen in **Figure 17** for E96W4 at 90 °C. If this type of discrepancy occurs within two plumes which have the same orientation, irrespective of gas chamber condition, temperature, fuel type, *etc.* the primary cause can be linked to in-nozzle differences from nucleation and cavitation, possibly due to geometric nozzle asymmetries or needle offset, linked with hole-to-hole variations.

As the temperature was gradually raised, each of the plumes increased in thickness due to enhanced breakup. When the temperature reached 90 °C at 0.5 bar gas pressure, it was possible to see the development of further vortical structures, especially for the upper middle plume, for all grades of hydrous ethanol. As the percentage of water was increased, both the upper and lower central plumes exhibited a change in the shape of plume tips. At the spray collapse condition of 110 °C, 0.5 bar, anhydrous ethanol still exhibited faint boundaries for each plume. As the percentage of water was increased from 4 to 15%, the plume boundaries became less clear to a point where it was no longer possible to distinguish between plumes B and C. The central section near the injector became 'whiter' showing a higher degree of droplets concentrating near the injector nozzle with increased Mie scattering. The plumes became wider and 'shorter' with a distinctive boundary between the outer section of each plume and the inner section. The outer section is where a higher degree of vaporisation can be seen, while within the inner section the droplets experience move towards the central axis to lower pressure regions leading gradually to spray collapse.

SPRAY STRUCTURE VARIATIONS

Standard deviation side-view spray images were produced at 777 µs ASOI over 100 injection events in **Figures 18–19** for 0.5 bar and 1.0 bar, respectively, to go hand in hand with the respective instantaneous side-view spray images presented earlier in **Figures 14–15**.

It is possible to observe comparable variations at 20 °C and 50 °C. Since each pair's plumes does not lie perfectly on top of one another as observed from the base view images, a concave like structure is observed from the side view perspective, leading to two sections of red colour regions at the tips indicating high intensity local fluctuations. However, the sharp interface along the plume boundaries at low temperatures shows consistent atomisation and no transient effect of plume flapping. At 110 °C, 1.0 bar gas pressure all fuels have plume boundaries with a greater degree of light blue colour indicating higher fluctuation along the plume boundaries as the temperature was increased. A higher degree of change in intensity is indicative of enhanced atomisation. When spray collapse conditions are produced, the blue colour shades typically observed between plumes B and C have completely disappeared for the alcohols. Instead, the higher local intensity differences spread across the lower parts of the merged plumes where the

mushrooming effect causes large differences in intensity values from injection to injection. The lighter tips shown earlier in the instantaneous spray images of *iso*-octane have resulted in higher values of standard deviation. This phenomenon has travelled further up the plume as atomisation occurs at the plume boundaries. The addition of water at 20 °C and 50 °C led to thinner plumes with increased local intensity differences that can be linked to inconsistent atomisation with larger droplets from injection to injection. The spray collapse condition of 110 °C, 0.5 bar also led to higher local intensity variations around the tip and perimeter of the spray, which could also be linked to enhanced atomisation.

Figures 20–21 display an array of standard deviation spray images at 777 µs ASOI for the base view for all temperatures and fuels for both 0.5 bar and 1.0 bar gas pressure, respectively. Differences become apparent when looking at the plume's colour between plume pair A compared to B and C between 20–50 °C. Plume pair A shows low differences in local intensity values from injection to injection as there are no red colour regions at the tips compared with the areas of red colour for plume pairs B and C. For all alcohols there is also a common trend of the upper central plume having a greater degree of standard deviation at these temperatures in both figures which indicates variations in plume-to-plume injections. At 90 °C, 0.5 and 1.0 bar the addition of water seems to reduce the standard deviation on the lower central plume.

Iso-octane displayed higher differences in local intensity at spray periphery and tips for each condition from injection to injection compared to all alcohols. This may be linked to better spray break-up of *iso*-octane with smaller droplets that behave more 'chaotically' from injection to injection. At 20 °C for 1.0 and 0.5 bar in the central bottom plume and at 50 °C and 0.5 bar in the top left plume the concave shape in a single plume can be observed. This correlates directly with some of the behaviour observed in the instantaneous spray images where the spray tips exhibited concave shapes especially for plumes B and C. It is also clear that at 110 °C, 0.5 bar, the plumes exhibit enhanced atomisation and vaporisation on the periphery close to the tips whilst maintaining their nominal geometrical orientation without plume merging, as indicated by the larger areas of yellow colour shades.

The effect of hole-to-hole variations from transient in-nozzle multiphase phenomena, coupled presumably to small geometrical asymmetries in nozzle holes and needle offset, can be seen by observing the difference for nominally symmetric holes of plume pairs. For example, in plume pair B of E96W4 at 110 °C, 0.5 bar there is a clear red region on the upper central plume which doesn't exist with the lower central plume as it has merged with the lower left plume at this condition.

SPRAY PLUME PENETRATION AND VELOCITY

Plume pair A has been selected for discussion here; however, penetration differences between pairs A, B and C are also commented on. The standard deviation over a series of 100 injections is indicated on penetration graphs by error bars. At 20 °C, 1.0 bar, in **Figure 22** *iso*-octane shows the same penetration to anhydrous ethanol at 777 µs ASOI, despite the slower start. Anhydrous ethanol is followed from the beginning of injection by the hydrous ethanol fuels in ascending order of water content. **Figure 23** shows the spray tip velocity at 20 °C, 1.0 bar. This was calculated by taking numerically the gradient of the penetration curve. The maximum velocity was observed at 555 µs ASOI, after which the velocity decreased and approached a plateau of about 60–70 m/s as a result of momentum being balanced by aerodynamic drag and fuel evaporation effects. The fuels with higher water content exhibit slower velocity on entry but sustain their velocity a little more than the less dense grades of hydrous ethanol. E100's large velocity can be attributed to the slight timing difference at which the spray first entered the chamber which was on some occasions at 333 µs ASOI. When decreasing the gas pressure to 0.5 bar at 20 °C in **Figure 24**, an approximate 4–10% increase in plume tip penetration was found during injection. The penetration at the last timing shown ranges from about 56–62 mm at 1.0 bar whereas this increases from about 58–65 mm when the fuels are injected into 0.5 bar. All forms of hydrous ethanol maintain a steady gradient until 666 µs ASOI and in order of their percentage of water.

When the temperature was raised to 50 °C at both 1.0 bar and 0.5 bar there was a clear increase in penetration compared to 20 °C. The reduction in liquid viscosity at higher temperature reduced friction losses, coupled possibly

to slightly enhanced cavitation effects due to the higher vapour pressure, resulted in faster exit velocity for all fuels at both gas pressures. **Figure 25** shows the plume tip penetration at 50 °C, 0.5 bar; the trends were the same at 1.0 bar. All fuels appeared one frame earlier at 333 µs ASOI instead of 444 µs ASOI. *Iso*-octane displays clearly larger penetration than the ethanol fuels. At 1.0 bar the levels of penetration follow a pattern that is once again in direct correlation with water content. However, E96W4 catches up with E100 by about 1 ms ASOI. Study of spray tip velocities showed that fuels at 50 °C and 20 °C behaved similarly overall, with the spray tip velocity at 50 °C being slightly higher.

When increasing the temperature to 90 °C at 1.0 bar in **Figure 26**, which is well beyond the boiling point of ethanol, rapid vaporisation starts to occur at the tips, leading to even lower liquid penetration. Moreover, the effects of viscosity have been reduced allowing all fuels to have very similar penetration lengths initially, mostly in 'order' of their viscosities, with *iso*-octane penetrating the furthest and E85W15 penetrating the least, the latter exhibiting ~7% reduced penetration in comparison to E100. Unlike at 50 °C there is a clear difference between E100 and E96W4. **Figure 27** shows that there was a more gradual increase in penetration velocity up to its peak value at about 555 µs ASOI; this was because penetration started about a frame earlier due to lower viscous friction inside the nozzle and presumably increased levels of cavitation due to higher vapour pressure. Tip velocities reduced to levels below 60 m/s earlier than 1 ms ASOI due to faster vaporisation. The more hydrous forms of ethanol sustained their velocity further than the less hydrous blends which can be seen through flatter gradient between 888–999 µs. The effect of reducing the gas pressure to 0.5 bar on penetration for 90 °C fuel temperature, *i.e.* increasing the superheat, can be seen in **Figure 28**. Once again, during the initial phase of spray formation and penetration, the injection pressure difference across the nozzle highly governs the behaviour of all fuels. Once the effects of plume convergence and initial signs of spray 'mushrooming' have started to occur, as shown earlier, penetration was reduced. E100 had the furthest penetration whereas E85W15 penetrated the least, with the rest of the hydrous blends in-between in correlation to their water content. *Iso*-octane showed the least difference compared to 50 °C.

Figures 29–30 show the plume tip penetration graphs at injector body temperature of 110 °C at 1.0 bar and 0.5 bar gas pressure, respectively. *Iso*-octane at 1.0 bar clearly towers above all the other fuels penetration data due to its lower viscosity and lower vapour pressure that has not really affected the nominal shape of the spray. At 666 µs ASOI it is still possible to see the less dense fuels having slightly higher values in penetration, but by 1110 µs ASOI the denser fuels have 'caught up' to the less dense fuels. The effect of aerodynamic drag is likely to be one of the causes of this observation as the denser fuels can sustain further their higher momentum, coupled with reduced transfer of momentum in the radial direction due to weaker breakup. At the spray collapse condition of 110 °C, 0.5 bar, *iso*-octane has a much faster initial penetration due to lower viscosity effects in-nozzle, whilst gradually shows a decrease in liquid penetration due to faster vaporisation at the plume tip. The respective spray tip velocities in **Figures 31–32** show that *iso*-octane 's higher boiling point and lower vapour pressure than the alcohols reflected in steeper acceleration with higher peak velocity at 555 µs ASOI and steeper deceleration after that. The denser hydrous ethanol fuels exhibited slower peak velocities between 555–666 µs ASOI at 0.5 bar and retained their velocity for longer, *i.e.* all fuels started off in ascending order of water content are completely reversed their order by 1 ms ASOI. It is also clear that *iso*-octane at 0.5 bar exhibited the highest recorded velocity, in excess of 110 m/s, and broke up faster after that with greatly reduced velocity that reached levels lower than 50 m/s, effects related to the lowest viscosity and surface tension of the fuels shown.

Plume-to-plume penetration analysis showed that plume pair A experienced greater retardation than plume pair B, while plume pair C experienced the least retardation. At 20 °C, 1.0 bar, plume pair C penetrated approximately 16% further than plume pair A by 1 ms ASOI. Plume pair B was ~12% faster than plume pair A. All effects due to differences in hole orientation were significantly reduced as the viscosity of the fuel was reduced by raising the fuel temperature. The degree of difference between plume penetration from different holes reduced further as the pressure was decreased. The hole with the most acute angle, plume pair A, showed greater change than plumes B and C.

SPRAY CONE ANGLE

Starting from the ambient condition of 20 °C, 1.0 bar, **Figure 33** illustrates that *iso*-octane had almost the same cone angle to anhydrous ethanol, just short of 94°. As the percentage of water in ethanol was increased to just 4%, the cone angle increased and remained roughly constant up to 10% water content. For 15% water content, the cone angle decreased to levels lower than anhydrous ethanol. This behaviour highlights the differences observed macroscopically in spray images for plume pair C. When the gas pressure was decreased to 0.5 bar at 20 °C, the cone angle slightly increased for all fuels. The largest value was measured for *iso*-octane, about 97°. The difference between anhydrous ethanol and the hydrous fuels at 0.5 bar was smaller than at 1.0 bar. The differences between the hydrous blends remained generally consistent, with E85W15 still exhibiting the lowest cone angle. At 50 °C, 1.0 bar, the cone angle increased for all fuels, especially for the alcohols, with the differences between anhydrous ethanol and the hydrous blends becoming more prominent. Interestingly the highest cone angle was recorded for E96W4, a feature that persisted when the pressure was dropped to 0.5 bar. In contrast, E85W15 exhibited the smallest cone angle of the hydrous blends but larger than E100. At 90°C, E96W4 showed a very clear increase in cone angle to levels in excess of 100°, distinctly larger than all other hydrous blends at both 1.0 bar and 0.5 bar. It is also interesting to note that throughout both 50 °C and 90 °C fuel temperatures, at both 1.0 bar and 0.5 bar gas pressures, there was a consistent dip in cone angle by the presence of 2% additional water in E94W6 whilst the levels consistently peaked again for E90W10 and decreased for E85W15. The biggest influence on cone angle diversity between fuels has been the breakup behaviour of plume pair C. Widening of plume pair C for E96W4 at 90 °C and 0.5 bar gas pressure was observed by close inspection of spray images, and values as high as 2–3% at 90 °C, 0.5 bar were recorded. The plume tip concave separation further exacerbated this point for E96W4; the cone angle of plume pair C visibly expanded and the plume tips became more rounded. This holds true for 90 °C, 1.0 bar as well but to a lesser extent. The effects were examined in detail by repeated measurements and by adopting a new control fuel blend consisting of anhydrous ethanol mixed with 10% distilled water. It was found that the cone angle results were almost identical to the original E90W10 throughout; similarly for penetration.

At 110 °C fuel temperature and 1.0 bar gas pressure, the spray cone angle was reduced for the majority of the fuels when compared to 90 °C, 0.5 bar. The spray collapse condition of 110 °C, 0.5 bar, displayed the smallest cone angles for all fuels. However, it was clear that the near-nozzle local cone angle swelling caused all the hydrous fuels to have a higher cone angle value downstream by ~5% when compared to E100. Overall, a reduction in spray cone angle of 3–7% was found for the alcohols in comparison to 20 °C, 1.0 bar. In contrast, *iso*-octane exhibited the largest difference between 20 °C and 90 °C at 0.5 bar, in excess of 10%, due to faster breakup and vaporisation whilst retaining its nominal geometrical orientation of spray plumes.

SPRAY AREA AND PERIMETER

Base view imaging allowed capturing a longer part of the injection event prior to the spray getting ‘clipped’ by the border of the optical window, thereby allowing to quantify changes up to the latest stages of injection. Both spray area and perimeter of the spray’s base view were calculated in order to study different measures of shape. The areas shown for 20 °C, 1.0 bar in **Figure 34** highlight that the footprint of the spray contracted when moving from anhydrous to hydrous ethanol fuels in ascending order of water content, reflecting the penetration behaviour. At the spray collapse condition of 110 °C, 0.5 bar shown in **Figure 35** *iso*-octane had the largest spray area between 0.8–1 ms ASOI of all fuels but beyond 1.2 ms ASOI this contracted to levels lower than anhydrous ethanol. The hydrous fuels exhibited very similar footprint areas, lower than anhydrous ethanol’s. E94W6 showed an additional contraction at the end of injection. The spray perimeters of the ethanol fuels at 20 °C, 1.0 bar in **Figure 36** show generally consistent behaviour with the areas, exhibiting also little change in gradient during injection. Anhydrous ethanol showed the same perimeter to *iso*-octane, despite the smaller respective area. **Figure 37** shows the spray perimeters at 110 °C, 0.5 bar. The largest factor governing the observed differences here is related to the degree of spray collapse for each fuel. The larger the effect of spray collapse, the lower the perimeter recorded at each time frame as plumes

merged and the liquid fuel formed a cloud in the middle of the chamber. Clearly, *iso*-octane retained its perimeter higher than all fuels and anhydrous ethanol exhibited larger perimeter than the hydrous blends. In an attempt to provide a better metrics of spray collapse, the area to perimeter ratio was calculated in **Figures 38–39** for 20 °C, 1.0 bar and 110 °C, 0.5 bar, respectively. The steep gradient at the beginning of injection reflects the growth of area with small perimeter as the individual plumes are forming. At 20 °C, 1.0 bar the ratio achieves gradually a fairly uniform level, particularly for the ethanol fuels. However, at 110 °C, 0.5 bar the increase in the value of this ratio for the ethanol fuels was smoother and maintained a steady gradient of increase during injection. This is because the spray structure becomes less 'finger-like' and more 'cloud-like'. There is a clear trend where the fuels with the more heavily collapsed sprays exhibit larger values of this ratio, providing an interesting single measure of the degree of spray collapse. More to the point, *iso*-octane maintains the lowest values of the ratio with weaker gradient of increase during injection.

DROPLET SMD AND VELOCITY

The SMD is shown in **Figure 40**. A range of 10–20 μm has been measured, depending on fuel and condition. The values shown have been quantified over the full injection duration; droplet sizes where as high as 60 μm when the leading edge of the plume went through the probe volume at the beginning of injection. It was found that *iso*-octane consistently had smaller droplets at all temperatures compared to all alcohols by about 7–11%. As the percentage of water increased from 4% to 15%, SMD generally increased. In particular, at 20 °C, 1.0 bar, 15% water presence in ethanol led to ~5% increase in SMD in comparison to anhydrous ethanol. E96W4 showed the largest difference in SMD when changing conditions; for example about 20% reduction occurred when increasing the temperature from 50 to 90 °C, 1.0 bar. Decreasing the pressure and increasing the temperature consistently reduced the SMD across all fuels. At 110 °C, 1.0 bar the SMD remained broadly constant by the addition of water to ethanol, whilst increasing the superheat further by dropping the pressure to 0.5 bar led to marginal increase in SMD when moving from 4% water to 15% water content in ethanol.

Droplet mean velocities are shown in **Figure 41**. The SMD and velocity showed an inverse correlation where a higher SMD was associated with lower velocity. At 20 °C and 50 °C, 1.0 bar, *iso*-octane had the fastest velocity by ~15%, compared to the alcohols. Between E96W4 and E90W10 there is minimal difference in velocities, with a slight increase for E90W10 once the boiling point of water has been surpassed. At higher fuel temperatures, increasing water content in ethanol showed an increase in droplet velocity between 3–16% for E85W15. In general, an increase in temperature and reduction in pressure led to a larger velocity, ~28% increase for E100, ~40% for E85W15 and ~30% for *iso*-octane between 20 °C, 1.0 bar and 110 °C, 0.5 bar conditions. The droplet velocities cannot be compared quantitatively directly with the plume tip velocities presented earlier. The values obtained by imaging represent the velocity of the droplets at the tip of the plume on a Lagrangian domain, whilst those obtained by PDA represent behaviour at a fixed point in space as the plume was passing through. Nevertheless, the general trends appear consistent and it is also noted that the droplets measured by PDA at the beginning of injection when the plume tip went through the probe volume had velocities very close to those quantified by high-speed spray imaging.

SUMMARY AND CONCLUSIONS

The current paper studied the effect of water content in ethanol on the mechanism of atomisation from a multi-hole injector at 20 °C, 50 °C, 90 °C, 110 °C fuel temperature at 1.0 bar and 0.5 bar gas pressure. Several fuels were tested, namely anhydrous ethanol (E100) and 4 hydrous ethanol fuels with 4–15% water content per volume (E96W4, E94W6, E90W10, E85W15), as well as *iso*-octane representing a typical mid-distillate of gasoline. Spray measurements were conducted by both high-speed spray imaging and droplet sizing. Moreover, the thermophysical properties of all fuels, including vapour pressure, density, viscosity and surface tension, as well as distillation curves, were obtained over a range of temperatures, and the Reynolds, Weber and Ohnesorge numbers were considered in the analysis. The main conclusions of this study are summarised as follows:

- As water content is increased the surface tension of hydrous ethanol increases and lies between that of anhydrous ethanol and water. However, the kinematic viscosity of hydrous ethanol increases to levels higher than that of anhydrous ethanol despite the fact that the kinematic viscosity of water is lower than that of anhydrous ethanol. The combination of higher surface tension with higher kinematic viscosity points to poorer spray breakup for hydrous ethanol due to lower Weber/higher Ohnesorge number effects.
- At 1.0 bar for 20°C anhydrous ethanol exhibited almost identical penetration to *iso*-octane. Adding water to ethanol reduced penetration in ascending order of water content, with E85W15 having shorter penetration than E100 by about 10%. E85W15 also exhibited the smallest cone angle. At higher temperatures up to 90 °C, anhydrous ethanol showed lower penetration than *iso*-octane whilst the hydrous fuels still exhibited lower penetration than that of anhydrous in sequence of increasing water content.
- When the gas pressure was reduced to 0.5 bar for 20 °C and 50 °C fuel temperature, the spray's outer cone angle widened and the plumes showed longer penetration. Hydrous ethanol fuels demonstrated larger spray cone angle than anhydrous ethanol. E96W4 which corresponded to the azeotropic point of ethanol water mixtures displayed the largest cone angle at all conditions, being distinctly higher than all other fuels at 90 °C.
- At 90 °C with 0.5 bar gas pressure and at 110 °C with 1.0 and 0.5 bar gas pressure the ethanol fuels showed signs of plume merging and spray collapse, with clear differences from *iso*-octane's higher penetration, particularly at 110 °C, 0.5 bar. Plume merging and collapse was stronger with increased water content. When increasing the fuel temperature from 90 °C to 110 °C at 0.5 bar, E96W4 exhibited the largest reduction in cone angle.
- The area and perimeter of the spray's base view footprint were calculated and the ratio of area to perimeter was used to probe the degree of spray collapse. The largest ratio values were recorded for *iso*-octane at 20 °C, 1.0 bar. At 110 °C, 0.5 bar the alcohols exhibited partial spray collapse, causing a much lower area to perimeter ratio than at 20 °C, distinctly lower than *iso*-octane's. Fuels with more heavily collapsed sprays at superheated conditions exhibited larger values of this ratio.
- *Iso*-octane had consistently smaller droplet SMD than the ethanol fuels. As the percentage of water increased there was an increase in SMD at all conditions. For all fuels, increasing the temperature and reducing the pressure decreased droplet sizes. E96W4 exhibited the largest differences in SMD when changing conditions, for example about 20% reduction when increasing the fuel temperature from 50 to 90 °C at 1.0 bar gas pressure. As the percentage of water increased from E96W4 to E85W15 there was an increase in SMD by up to 5% over the range of conditions studied.

In summary, levels of 4% water content (azeotrope) appeared interesting as they led broadly to the same spray penetration to anhydrous ethanol, with enhanced cone angle and no deleterious effect on droplet sizes. At the highest fuel temperature, the most hydrous ethanol blend tested, of 15% water, exhibited the most signs of gradual spray collapse and some favourable effects in droplet sizes. These two blends can provide direction for further work.

ACKNOWLEDGEMENTS

The authors would like to thank the UK's Engineering and Physical Sciences Research Council (EPSRC) for financial support and Shell Global Solutions (UK) Ltd. for financial and technical support.

REFERENCES

1. Lopes, M.L., Christina de Lima Paulillo, S.C., Godoy, A., Cherubin, R.A., Lorenzi, M.S., Carvalho Giometti, F.H., Domingos Bernardino, C., de Amorim Neto, H.B, de Amorim, H.V. [2016], Ethanol production in Brazil: A bridge between science and industry, Brazilian Journal of Microbiology, Vol. 47, pp. 64–76.
2. Luchansky M.S., Monks J. [2009], Supply and demand elasticities in the US ethanol fuel market, Energy Economics, Vol. 31, pp. 403–410.
3. Han, J., Somers, L.M.T., Cracknell, R.F., Joedicke, A., Wardle, R., Mohan, V.R.R. [2020], Experimental investigation of ethanol/diesel dual-fuel combustion in a heavy-duty diesel engine, Fuel, Vol. 275, 117867.

4. Leach, C.P.F., Stone, R., Richardson, D., Turner, J.W.G., Lewis, A., Akehurst, S., Remmert, S., Campbell, S., Cracknell, R.F. [2018], The effect of oxygenate fuels on PN emissions from a highly boosted GDI engine, Fuel, Vol. 225, pp. 277–286.
5. Kabasin, D.F., Hurter, T., Lamers, R., Hoyer, K., Kazour, J. [2009], Heated injectors for ethanol cold starts, SAE Paper 2009-01-0615.
6. Sileghem, L., Casier, B., Coppens, A., Vancoillie J., Verhelst, S. [2014], Influence of water content in ethanol-water blends on the performance and emissions of an SI engine. Proceedings of FISITA World Automotive Congress, June 2–6, 2014, Maastricht, Netherlands.
7. Munsin, R., Laoonual, Y., Jugjai, S., Imai, Y. [2013], An experimental study on performance and emissions of a small SI engine generator set fuelled by hydrous ethanol with high water contents up to 40%, Fuel, Vol. 106, pp. 586–592.
8. Khatiwada, D., Venkata, B. K., Silveira, S., Johnson, F.X. [2016], Energy and GHG balances of ethanol production from cane molasses in Indonesia, Applied Energy, Vol. 164, pp. 756–768.
9. Bansal, A., Illukpitiya, P., Tegegne, F., Singh, S.P. [2016], Energy efficiency of ethanol production from cellulosic feedstock, Renewable and Sustainable Energy Reviews, Vol. 58, pp. 141–146.
10. Lawson, K.W., Lloyd, D.R., [1997] Membrane distillation, Journal of Membrane. Science, Vol. 124, pp. 1–25.
11. Pacheco-Basulto, J.A., Hernández-McConville, D., Barroso-Muñoz, F.O., Hernández S., Segovia-Hernández J. G., Castro-Montoya, A.J., Bonilla-Petriciolet, A. [2012], Purification of bioethanol using extractive batch distillation: Simulation and experimental studies, Chemical Engineering and Processing: Process Intensification, Vol. 61, pp. 30–35.
12. Shapouri, H., Duffield, J.A., Wang, M.Q. [2002], The energy balance of corn ethanol: An update, Agricultural Economic Report, Number 813, United States Department of Agriculture.
13. Martinez-Frias, J., Aceves, S.M., Flowers, D.L. [2007], Improving ethanol life cycle energy efficiency by direct utilization of wet ethanol in HCCI engines, Journal of Energy Resources Technology, Vol. 129, pp. 332–337.
14. Schifter, I., Diaz, L., Gómez, J., Gonzalez, U. [2013], Combustion characterization in a single cylinder engine with mid-level hydrated ethanol–gasoline blended fuels, Fuel, Vol. 103, pp. 292–298.
15. Deng X., Chen Z., Wang X., Zhen H., Xie R. [2018], Exhaust noise, performance and emission characteristics of spark ignition engine fuelled with pure gasoline and hydrous ethanol gasoline blends, Case Studies in Thermal Engineering, Vol. 12, pp. 55–63.
16. Duncan, B.N., Prados, A.I., Lamsal, L.N., Liu, Y., Streets, D.G., Gupta, P., Hilsenrath, E., Kahn, R.A., Nielsen, J.E., Beyersdorf, A.J. [2014], Satellite data of atmospheric pollution for US air quality applications: Examples of applications, summary of data end-user resources, answers to FAQs, and common mistakes to avoid, Atmospheric environment, Vol. 94, pp. 647–662.
17. Wang, X., Chen, Z., Ni, J., Liu, S., Zhou, H. [2015], The effects of hydrous ethanol gasoline on combustion and emission characteristics of a port injection gasoline engine, Case Studies in Thermal Engineering, Vol. 6, pp. 147–154.
18. Fagundez, J., Sari, R., Mayer, F., Martins, M., Salau, N. [2017], Determination of optimal wet ethanol composition as a fuel in spark ignition engine, Applied Thermal Engineering, Vol. 112, pp. 317–325.
19. Augoye, A., Aleiferis, P.G. [2014], Characterization of flame development with hydrous and anhydrous ethanol fuels in a spark-ignition engine with direct injection and port injection systems. SAE Paper 2014-01-2623.
20. Koupaie, M.M., Cairns, A., Vafamehr, H., Lanzanova, T.D.M. [2019], A study of hydrous ethanol combustion in an optical central direct injection spark ignition engine, Applied Energy, Vol. 237, pp. 258–269.
21. Lanzanova, T.D.M., Dalla Nora, M., Zhao, H. [2016], Performance and economic analysis of a direct injection spark ignition engine fueled with wet ethanol, Applied Energy, Vol. 169, pp. 230–239.

22. Hinton, N., Stone, R., Cracknell, R.F., Olm, C. [2018], Aqueous ethanol laminar burning velocity measurements using constant volume bomb methods, Fuel, Vol. 214, pp. 127–134.
23. Garzón Lama, L., Sotton, J., Martins, C.A. [2020], Experimental burning velocities of ethanol-water-air at elevated pressure and temperature, Fuel, Vol. 265, 116933.
24. Balabin, R.M., Syunyaev, R.Z. and Karpov, S.A. [2007], Quantitative Measurement of Ethanol Distribution over Fractions of Ethanol-Gasoline Fuel, Energy and Fuels, Vol. 21, pp. 2460–2465, 2007.
25. Kar, K., Last, T., Haywood, C. and Raine, R.R. [2008], Measurement of Vapour Pressures and Enthalpies of Vaporisation of Gasoline and Ethanol Blends and their Effects on Mixture Preparation in an SI Engine, SAE Paper 2008-01-0317.
26. Price, C., Hamzehloo, A., Aleiferis, P.G., Richardson, D. [2016], An Approach to Modelling Flash-Boiling Fuel Sprays for Direct-Injection Spark-Ignition Engines, Atomization and Sprays, Vol. 26, pp. 1197–1239.
27. Price, C., Hamzehloo, A., Aleiferis, P.G., Richardson, D. [2018], Numerical Modelling of Fuel Spray Formation and Collapse from Multi-Hole Injectors under Flash-Boiling Conditions, Fuel, Vol. 221, pp. 518–541.
28. Price, C, Hamzehloo, A., Aleiferis, P.G., Richardson, D. [2020], Numerical Modelling of Droplet Breakup for Flash-Boiling Fuel Spray Predictions, International Journal of Multiphase Flow, Vol. 125, 103183.
29. Butcher, A.J., Aleiferis, P.G., Richardson, D. [2013], Development of a real-size optical injector nozzle for studies of cavitation, spray formation and flash-boiling at conditions relevant to direct-injection spark-ignition engines, International Journal of Engine Research, Vol. 14, pp. 557–577.
30. Butcher, A., Aleiferis, P.G., Richardson, D. [2015], Characterisation of Spray Development from Spark-Eroded and Laser-Drilled Multi-Hole Injectors in an Optical DISI Engine and in a Quiescent Injection Chamber. SAE Paper 2015-01-1903.
31. van Romunde, Z.R., Aleiferis, P.G., Cracknell, R.F., Walmsley, H.L. [2007], Effect of fuel properties on spray development from a multi-hole DISI engine injector, SAE Transactions, Journal of Engines, Vol. 116, pp. 1313–1331, SAE Paper 2007-01-4032.
32. van Romunde, Z.R. and Aleiferis, P.G. [2009], Effect of Operating Conditions and Fuel Volatility on Development and Variability of Sprays from Gasoline Direct-Injection Multi-Hole Injectors Atomization and Sprays, Vol. 19, pp. 207–234.
33. Aleiferis, P.G., van Romunde, Z.R. [2013], An Analysis of Spray Development with iso-Octane, n-Pentane, Gasoline, Ethanol and n-Butanol from a Multi-Hole Injector under Hot Fuel Conditions, Fuel, Vol. 105, pp. 143–168.
34. Serras-Pereira, J., Aleiferis, P.G., Richardson, D., Wallace, S. [2007], Mixture formation and combustion variability in a spray-guided DISI engine, SAE Transactions, Journal of Engines 116, pp. 1332–1356, SAE Paper 2007-01-4033.
35. Serras-Pereira, J., Aleiferis, P.G., Richardson, D., Wallace, S. [2008], Characteristics of Ethanol, Butanol, Iso-Octane and Gasoline Sprays and Combustion from a Multi-Hole Injector in a DISI Engine. SAE International Journal of Fuels and Lubricants, Vol. 1, pp. 893–909, SAE Paper 2008-01-1591.
36. Serras-Pereira, J., Aleiferis, P.G., Richardson, D. [2011], Imaging and Heat Flux Measurements of Wall Impinging Sprays of Hydrocarbons and Alcohols in a Direct-Injection Spark-Ignition Engine, Fuel, Vol. 91, pp. 264–297.
37. Aleiferis, P.G., Serras-Pereira, J., Walmsley, H.L., Davies, T.J., Cracknell, R.F. [2013], Heat Flux Characteristics of Spray Wall Impingement with Ethanol, Butanol, iso-Octane, Gasoline and E10 Fuels, International Journal of Heat and Fluid Flow, Vol. 44, pp. 662–683.

38. Serras-Pereira, J., Aleiferis, P.G., Richardson, D. [2014], An Experimental Database on the Effects of Single- and Split-Injection Strategies on Spray formation and Spark Discharge in an Optical Direct-Injection Spark-Ignition Engine Fuelled with Gasoline, iso-Octane and Alcohols, International Journal of Engine Research, Vol. 16, pp 851–896.
39. Price, C., Hamzehloo, A., Aleiferis, P.G., Richardson, D. [2016], An Approach to Modelling Flash-Boiling Fuel Sprays for Direct-Injection Spark-Ignition Engines, Atomization and Sprays, Vol. 26, pp. 1197–1239.
40. Price, C., Hamzehloo, A., Aleiferis, P.G., Richardson, D. [2018], Numerical Modelling of Fuel Spray Formation and Collapse from Multi-Hole Injectors under Flash-Boiling Conditions, Fuel, Vol. 221, pp. 518–541.
41. Price, C, Hamzehloo, A., Aleiferis, P.G., Richardson, D. [2020], Numerical Modelling of Droplet Breakup for Flash-Boiling Fuel Spray Predictions, International Journal of Multiphase Flow, Vol. 125, 103183.
42. Gandhi, A. H., Meinhart, M. [2009], "Fuel Injector Flow Rate Analysis for the Duratec 35 EcoBoost Engine", SAE Paper 2009-01-1505.
43. Albrecht, H.-E., Damaschke, N., Borys, M., Tropea, C. [2013], Laser Doppler and Phase Doppler Measurement Techniques, Springer.
44. Aleiferis, P.G., Serras-Pereira, J., van Romunde Z.R., Caine, J., Wirth, M. [2010], Mechanisms of spray formation and combustion from a multi-hole injector with E85 and gasoline, Combustion and Flame, Vol. 157, pp. 735–756.
45. Behringer, M.K., Aleiferis, P.G., OudeNijeweme, D., Freeland, P. [2014], Spray formation from spark-eroded and laser-drilled injectors for DISI engines with gasoline and alcohol fuels, SAE international journal of fuels and lubricants, Vol. 7, pp. 803–822.
46. Aleiferis, P.G., Behringer, M.K., OudeNijeweme, D., Freeland, P. [2015], Spray Imaging and Droplet Sizing of Spark-Eroded and Laser-Drilled Injectors with Gasoline-Butanol and Gasoline-Ethanol Blends, International Conference on Fuel Systems for IC Engines, pp. 179–198, March 10-11, 2015, IMechE, London, UK.
47. Hoppe, F., Thewes, M., Baumgarten, H., Dohmen, J. [2016], Water injection for gasoline engines: Potentials, challenges, and solutions, International Journal of Engine Research, Vol. 17, pp. 86–96.
48. Iacobacci, A., Marchitto, L., Valentino, G. [2017], Water Injection to Enhance Performance and Emissions of a Turbocharged Gasoline Engine under High Load Condition, SAE Paper 2017-01-0660.
49. Mingrui, W., Sa, N.T., Turkson, R.F., Jinping, L. Guanlun, G. [2017], Water injection for higher engine performance and lower emissions, Journal of the Energy Institute, Vol. 90, pp. 285–299.
50. Raut, A., Mallikarjuna, J.M. [2019], Effects of direct water injection and injector configurations on performance and emission characteristics of a gasoline direct injection engine: A computational fluid dynamics analysis, International Journal of Engine Research, Vol. 21, pp. 1520–1540.
51. Cordier, M., Lecompte, M., Malbec, L.-M., Reveille, B., Servant, C., Souidi, F., Torcolini, N. [2019], Water Injection to Improve Direct Injection Spark Ignition Engine Efficiency, SAE Paper 2019-01-1139.
52. Yaws, C.L. [2003], Yaws' Handbook of Thermodynamic and Physical Properties of Chemical Compounds, Knovel.
53. NIST Reference Fluid Thermodynamic and Transport Properties Database [2020], National Institute of Standards and Technology, USA, https://www.nist.gov/srd/refprop.
54. González, B., Calvar, N., Gómez, E., Domínguez, A. [2007], Density, dynamic viscosity, and derived properties of binary mixtures of methanol or ethanol with water, ethyl acetate, and methyl acetate at T = 293.15, 298.15, and 303.15 K, Journal of Chemical Thermodynamics, Vol. 39, pp. 1578–1588.
55. Khattab, I.S., Bandarkar, F., Amin, M., Fakhree, A., Jouyban, A. [2012], Density, viscosity, and surface tension of water+ethanol mixtures from 293 to 323 K, Korean Journal of Chemical Engineering, Vol. 29, pp. 812–817.

56. Pires, R.M., Costa, H.F., Ferreira, A.G.M., Fonseca, I.M.A. [2007], Viscosity and Density of Water + Ethyl Acetate + Ethanol Mixtures at 298.15 K and 318.15 K and Atmospheric Pressure, Journal of Chemical Engineering Data, Vol. 52, pp. 1240–1245.
57. Ohnesorge, W. [1931], Die Bildung von Tropfen an Düsen und die Auflösung flüssiger Strahlen. Zeitschrift für Angewandtw Mathmatik und Mechanik, Bd. 16, Heft 6, pp 355–358.
58. Reitz, R.D., Bracco, F.V. [1982], Mechanisms of Atomization of a Liquid Jet, Physics of Fluids, Vol. 25, pp. 1730–42.
59. Aleiferis, P.G., Shukla, J., Brewer, M., Cracknell, R.F. [2021], Spray Development of *iso*-Octane, Ethanol, Hydrous Ethanol and Water from a Multi-Hole Injector under Ultra Cold Fuel Temperature Conditions, Fuel, in Print.
60. Serras-Pereira, J., van Romunde, Z.R., Aleiferis, P.G, Richardson, D., Wallace, S., Cracknell, R.F. [2010], Cavitation, primary break-up and flash boiling of gasoline, iso-octane and n-pentane with a real-size optical direct-injection nozzle, Fuel, Vol. 89 (2010) 2592–2607.
61. Aleiferis, P.G., Serras-Pereira, J., Augoye, A., Davies, T.J., Cracknell, R.F., Richardson, D. [2010], Effect of Fuel Temperature on In-Nozzle Cavitation and Spray Formation of Liquid Hydrocarbons and Alcohols from a Real-Size Optical Injector for Direct-Injection Spark-Ignition Engines, International Journal of Heat and Mass Transfer, Vol. 53, pp. 4588–4606.

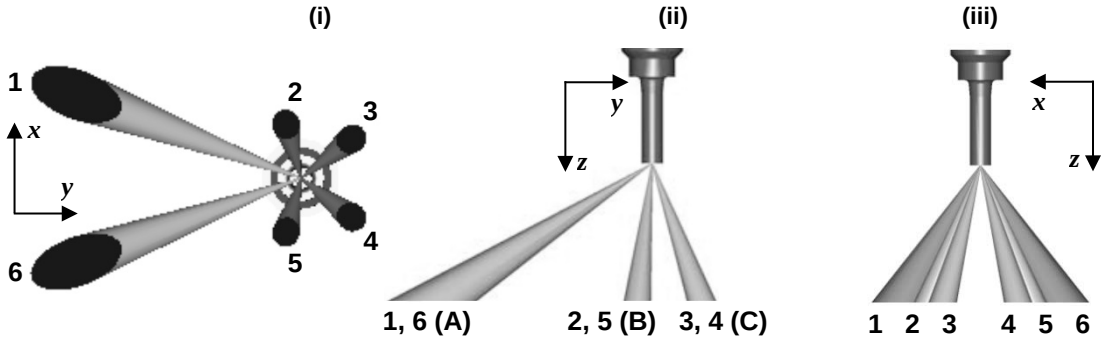

Figure 1. Schematic of injector and spray plumes: (i) base view, (ii) side view, (iii) end view.

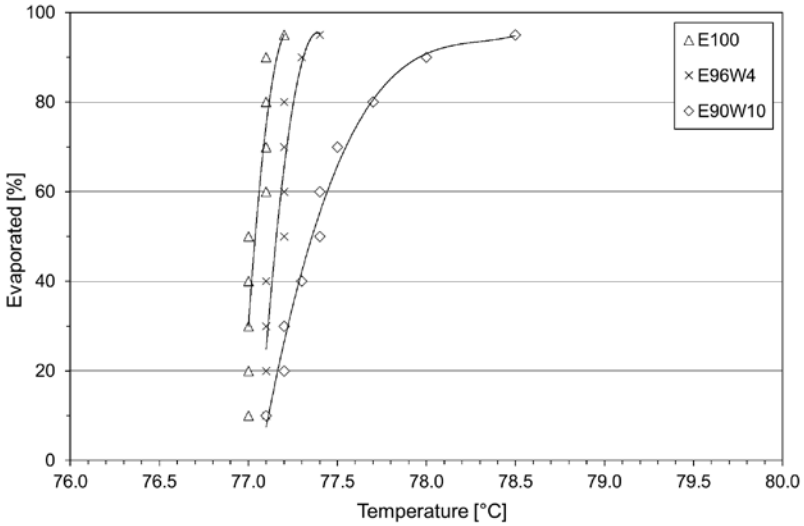

Figure 2. Distillation curves for anhydrous and hydrous ethanol.

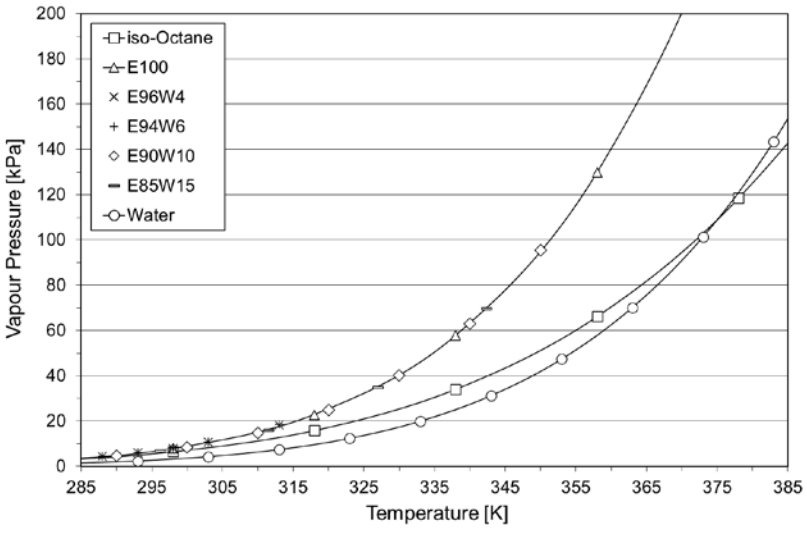

Figure 3. Vapour pressure for all fuels and water across various temperatures.

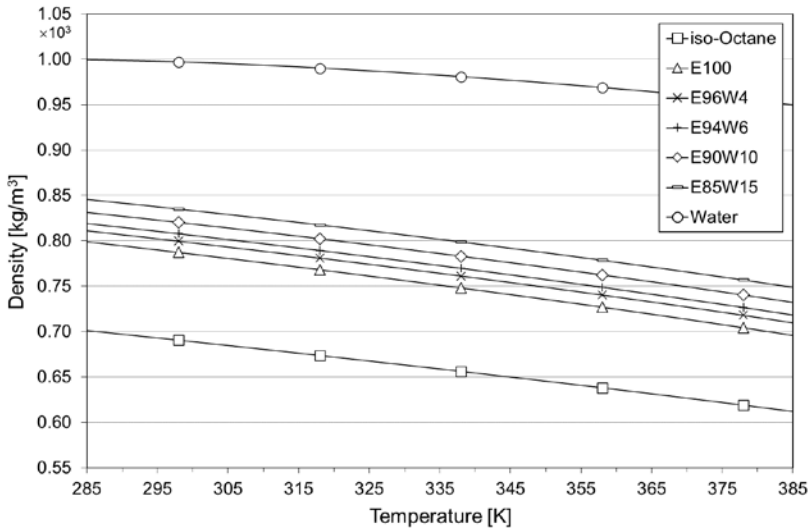

Figure 4. Density for all fuels and water across various temperatures.

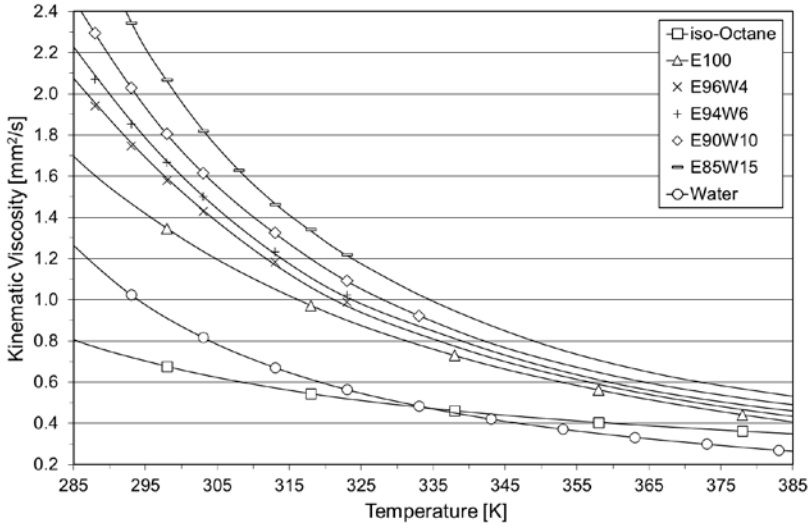

Figure 5. Kinematic viscosity for all fuels and water across various temperatures.

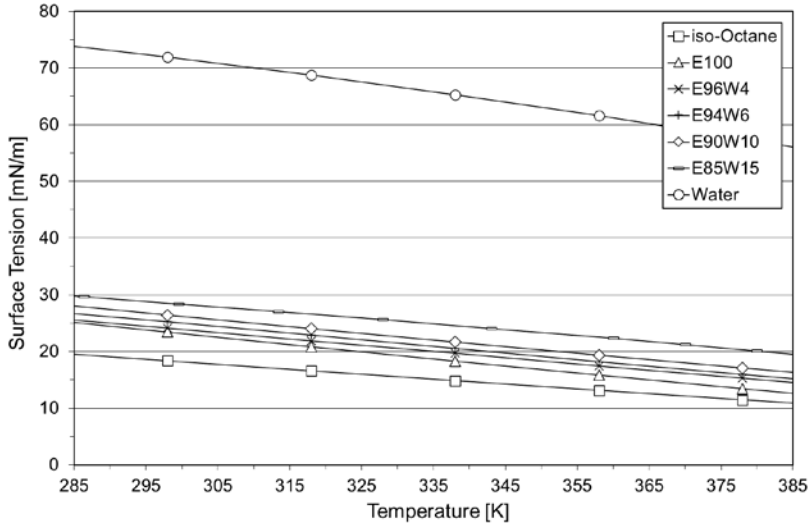

Figure 6. Surface tension for all fuels and water across various temperatures.

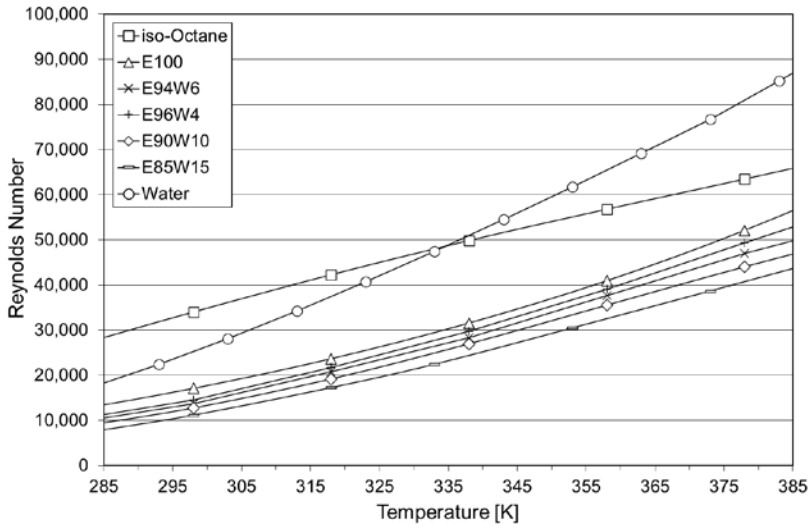

Figure 7. Reynolds number for all fuels and water across various temperatures.

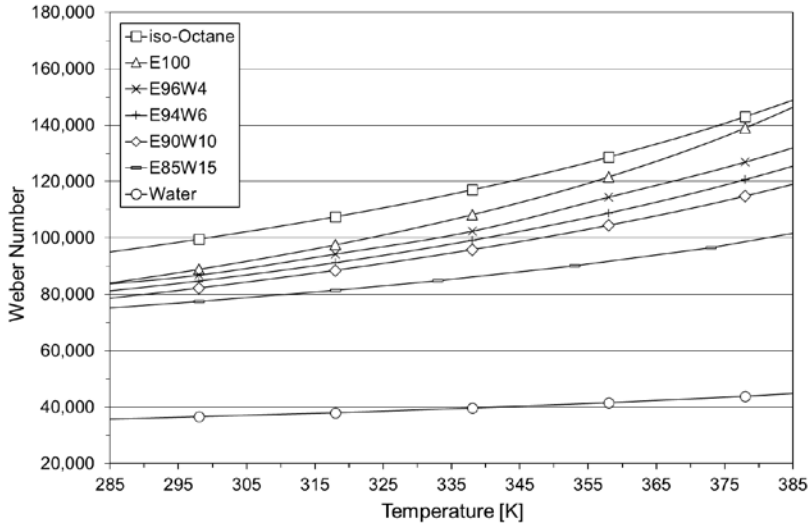

Figure 8. Weber number for all fuels and water across various temperatures.

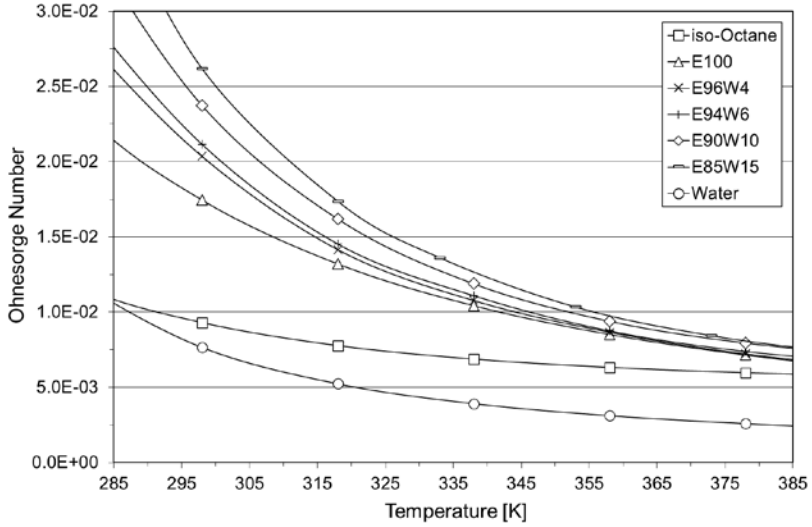

Figure 9. Ohnesorge number for all fuels and water across various temperatures.

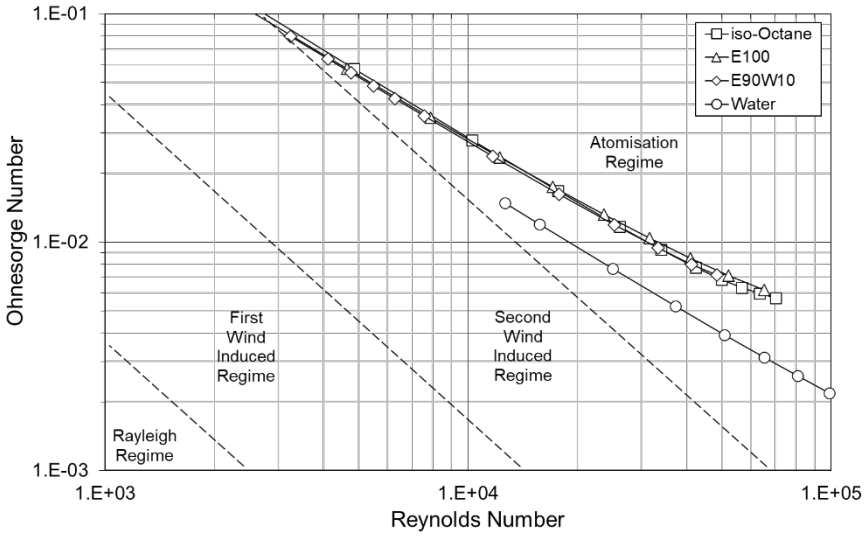

Figure 10. Ohnesorge atomisation diagram, all fuels and water.

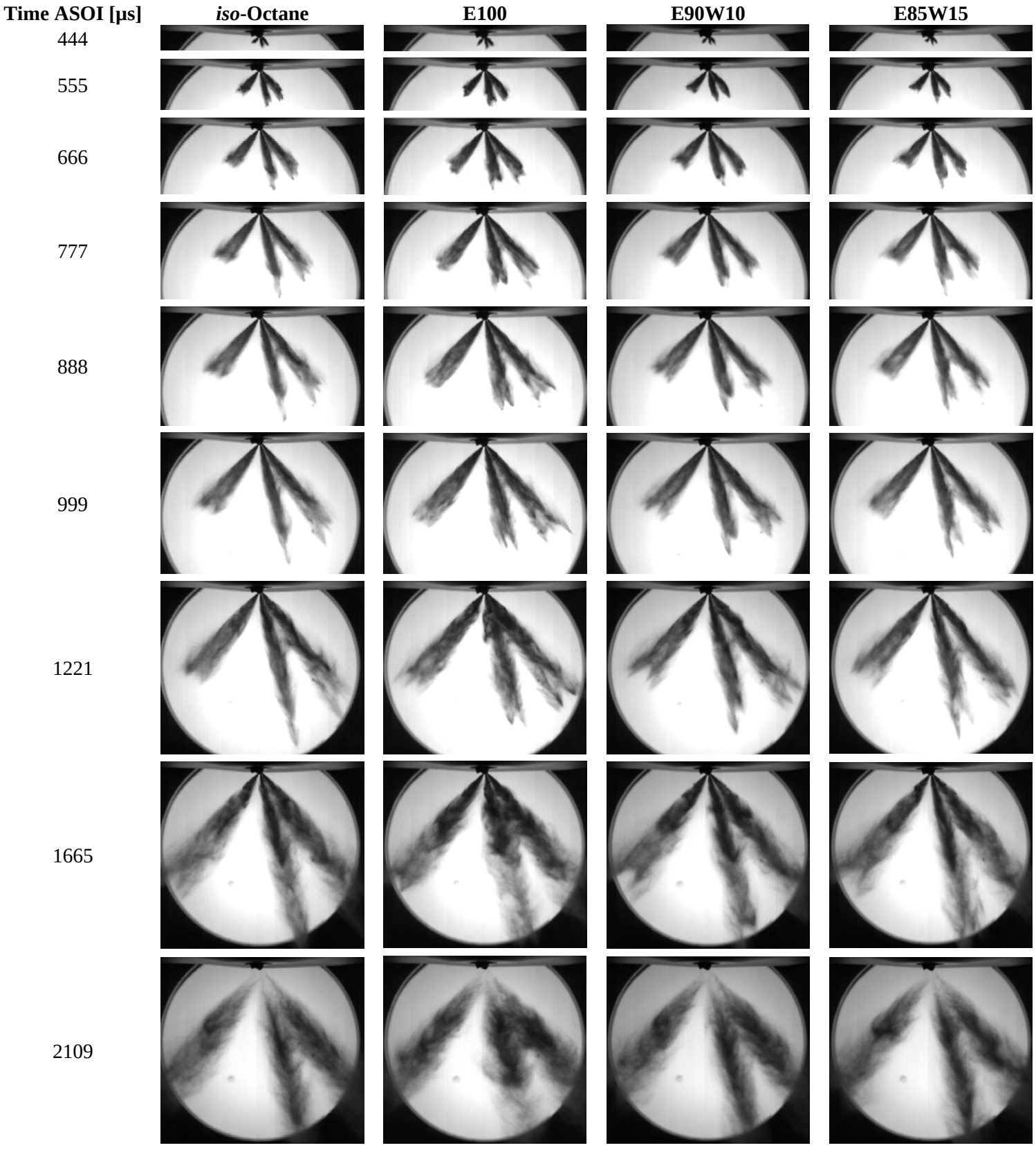

Figure 11. Spray Development of various fuels using side view at 20 °C, 1.0 bar.

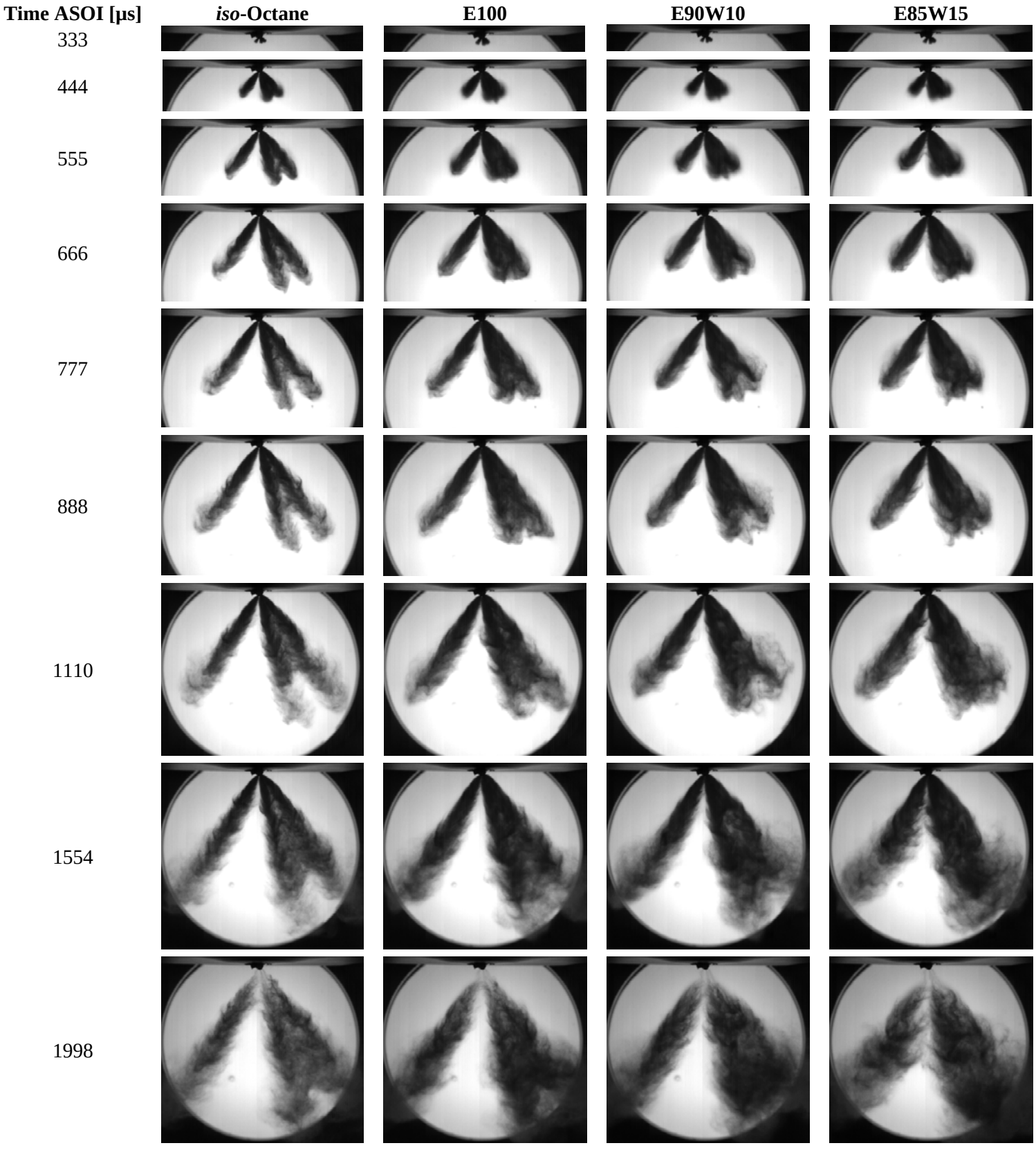

Figure 12. Spray Development of various fuels using side view at 110 °C, 0.5 bar.

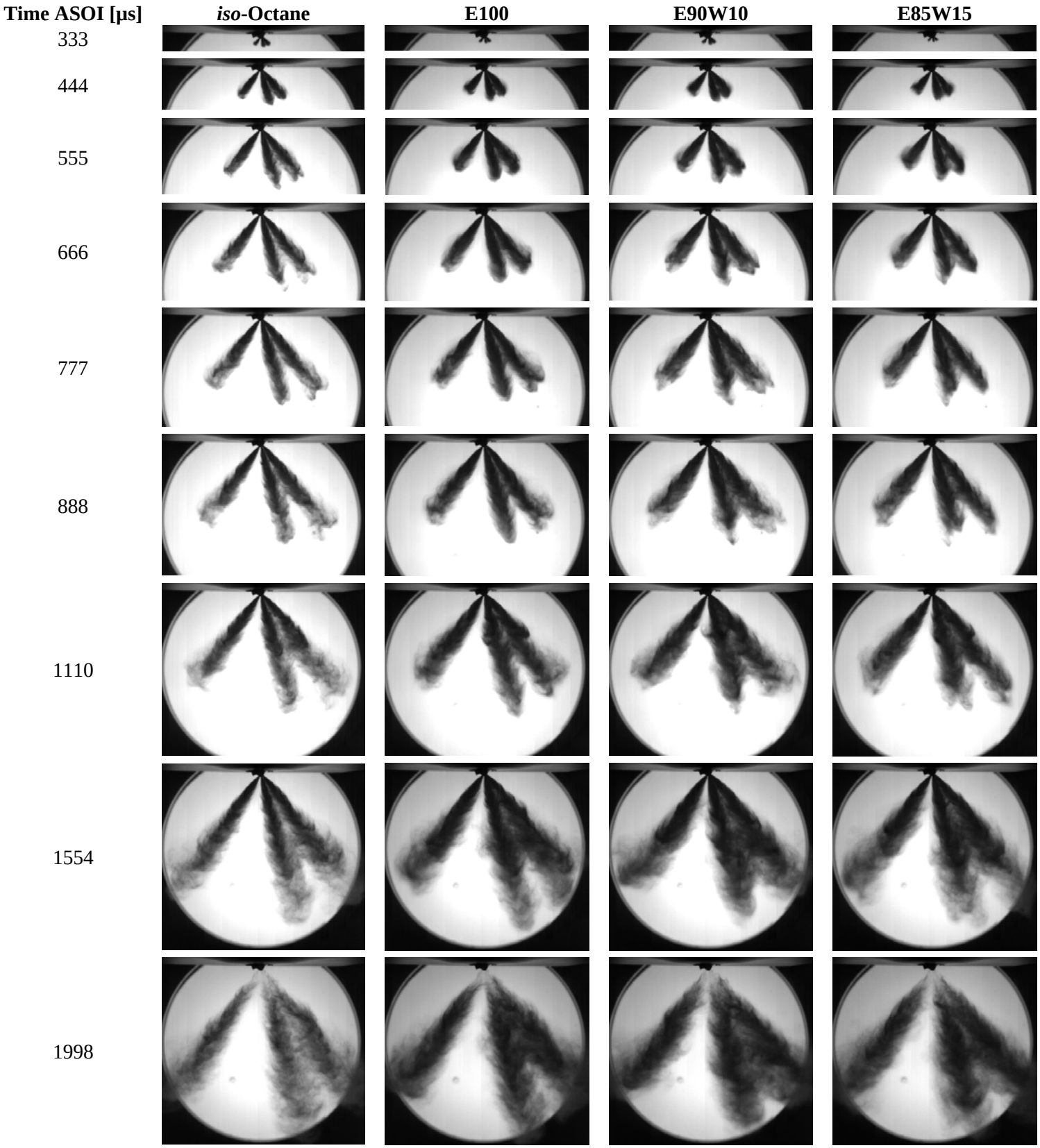

Figure 13. Spray Development of various fuels using side view at 110 °C, 1.0 bar.

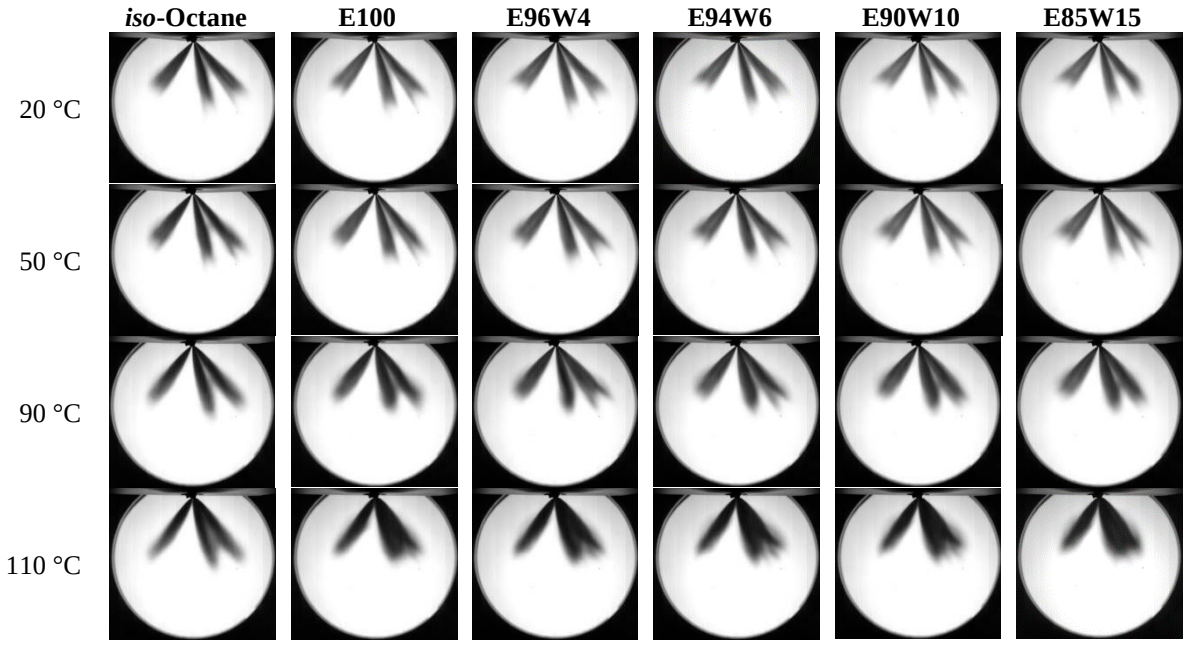

Figure 14. Side view mean spray images, all fuels and temperatures, 0.5 bar, 777 µs ASOI.

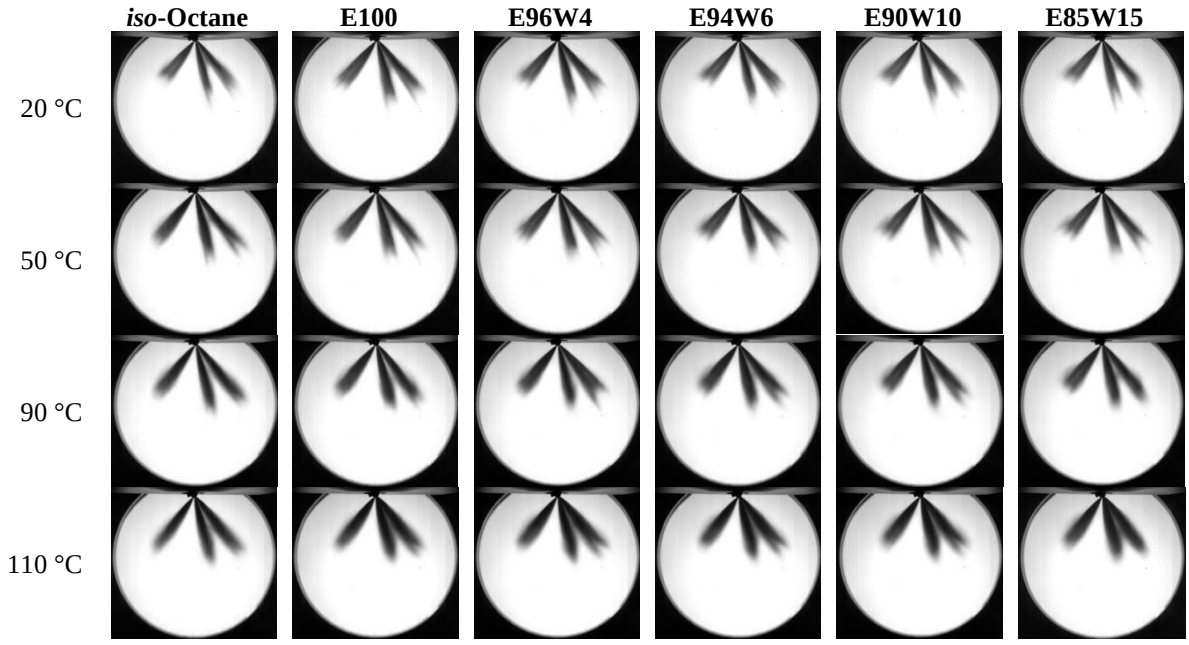

Figure 15. Side view mean spray images, all fuels and temperatures, 1.0 bar, 777 µs ASOI.

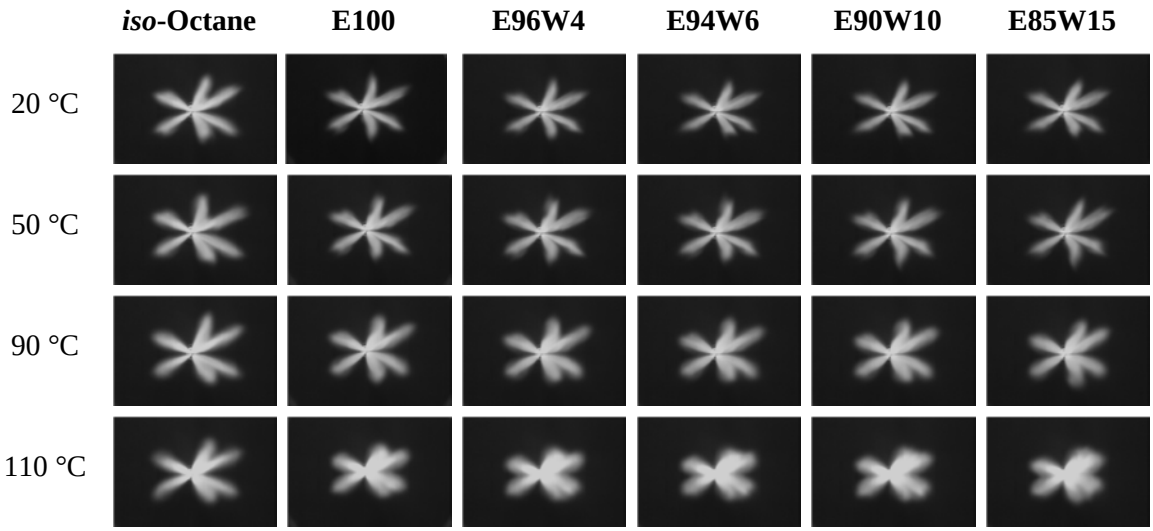

Figure 16. Base view mean spray images, all fuels and temperatures, 0.5 bar, 777 µs ASOI.

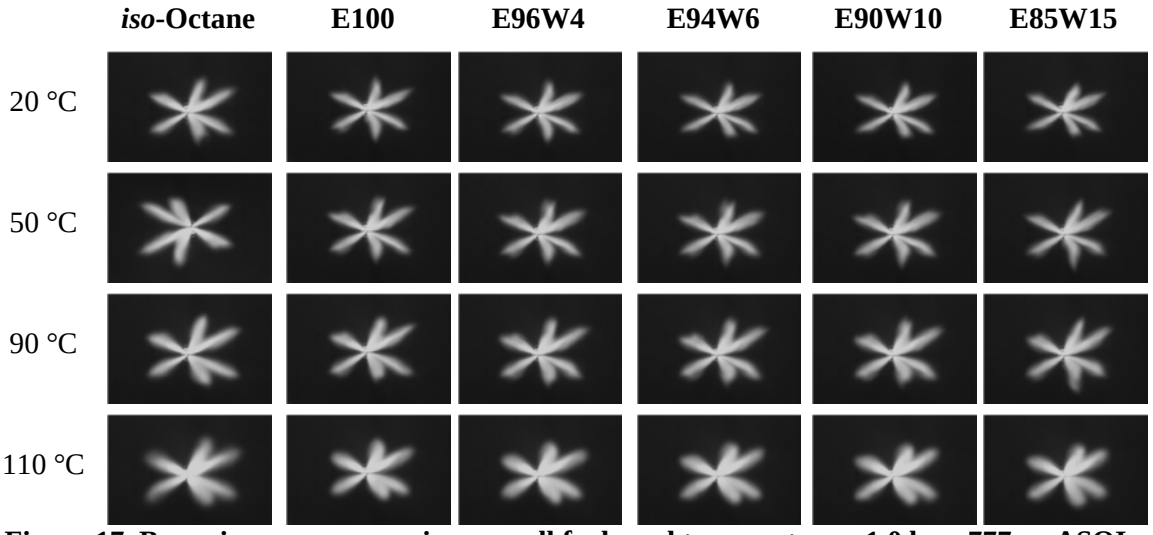

Figure 17. Base view mean spray images, all fuels and temperatures, 1.0 bar, 777 µs ASOI.

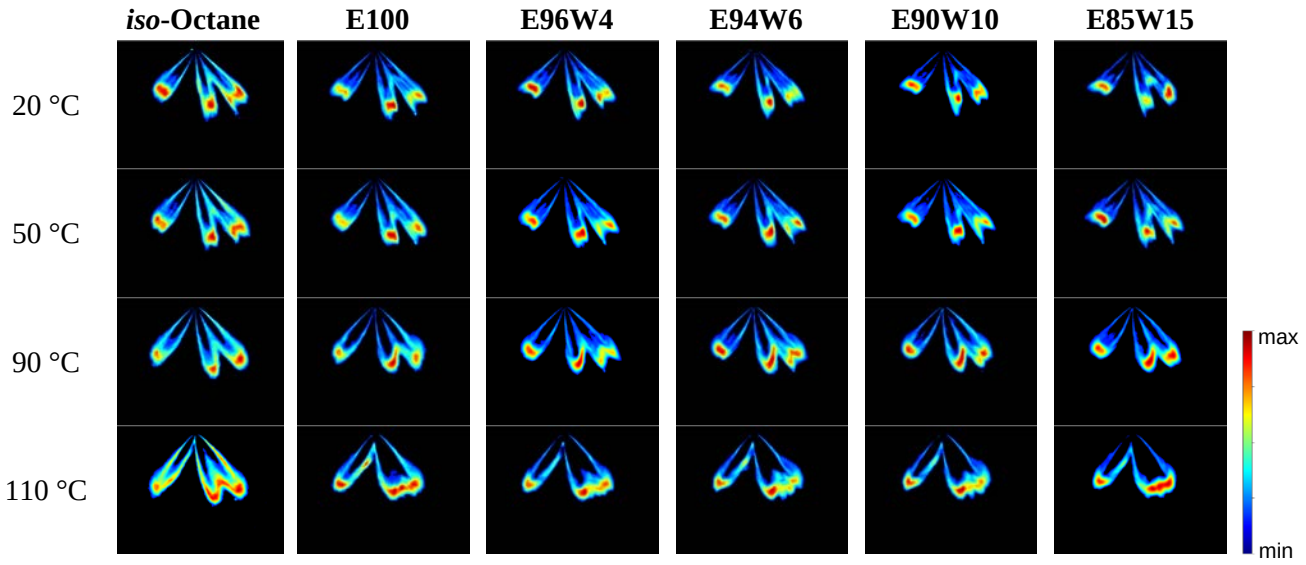

Figure 18. Side view standard deviation spray images, all fuels and temperatures, 0.5 bar, 777 µs ASOI.

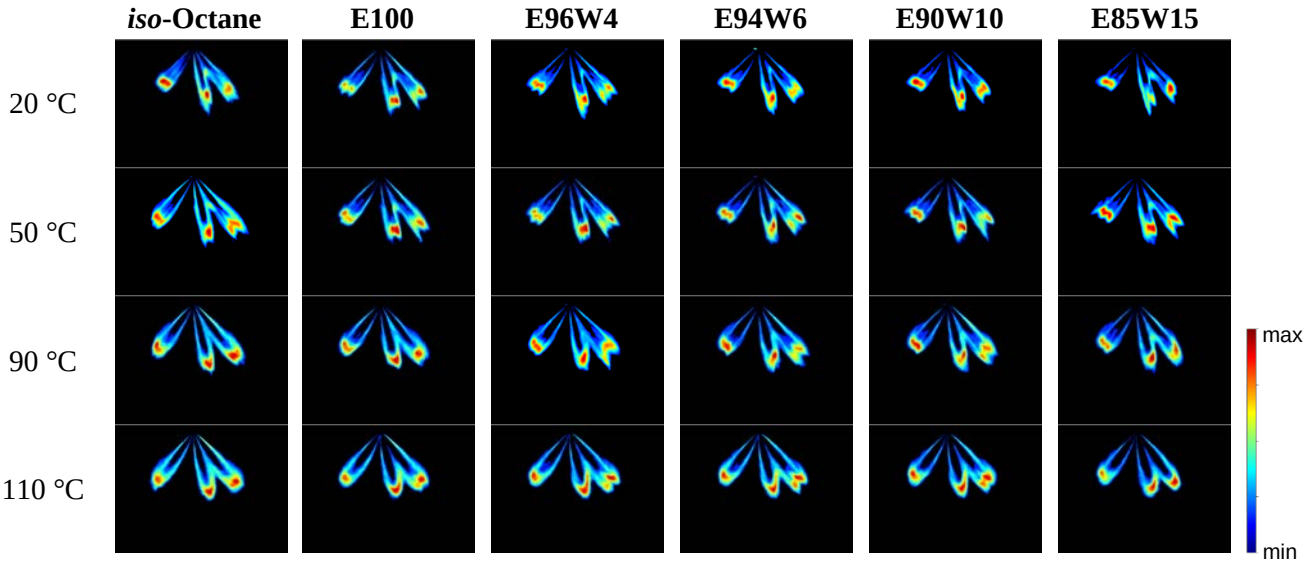

Figure 19. Side view standard deviation spray images, all fuels and temperatures, 1.0 bar, 777 µs ASOI.

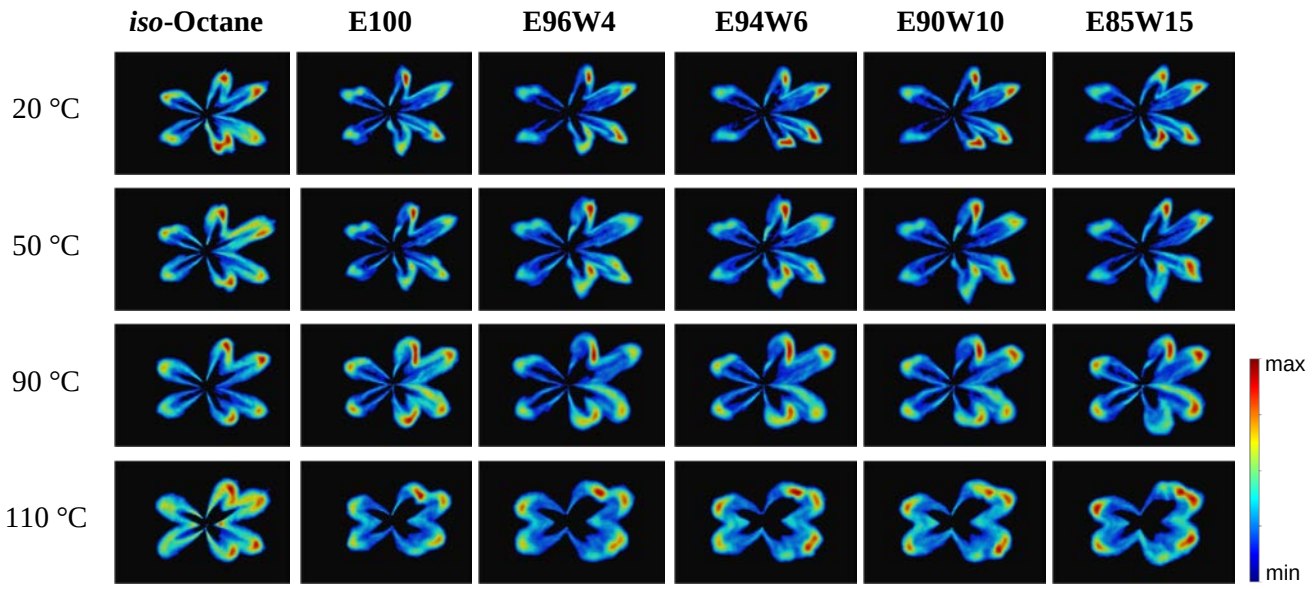

Figure 20. Base view standard deviation spray images, all fuels and temperatures, 0.5 bar, 777 µs ASOI.

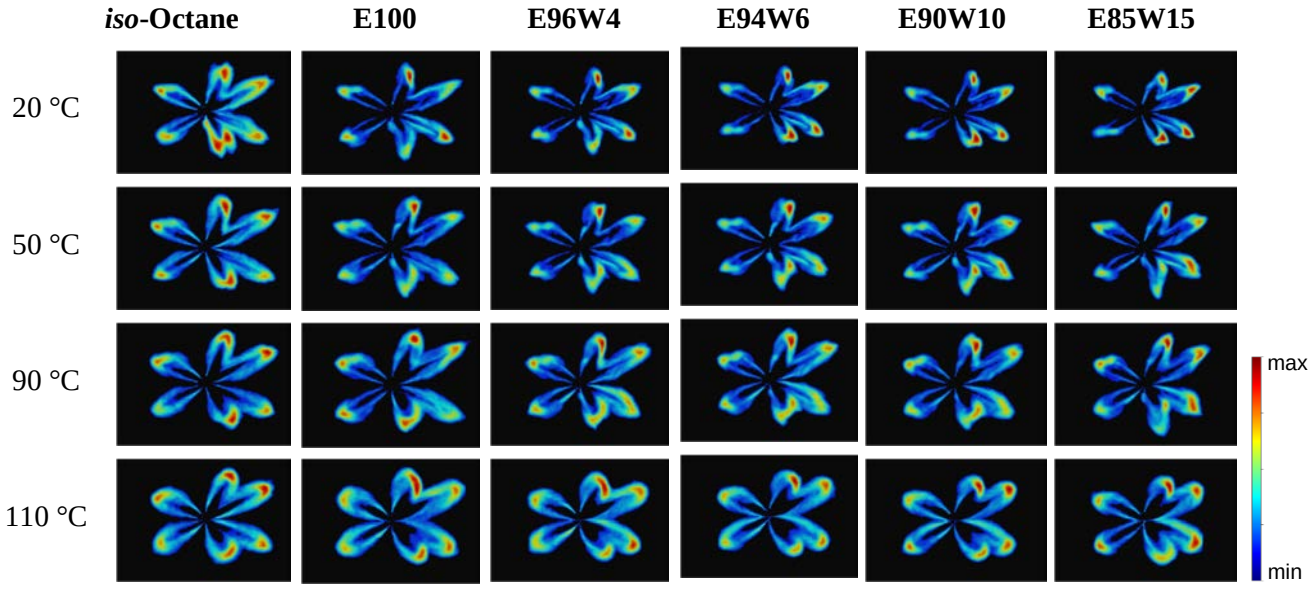

Figure 21. Base view standard deviation spray images, all fuels and temperatures, 1.0 bar, 777 µs ASOI.

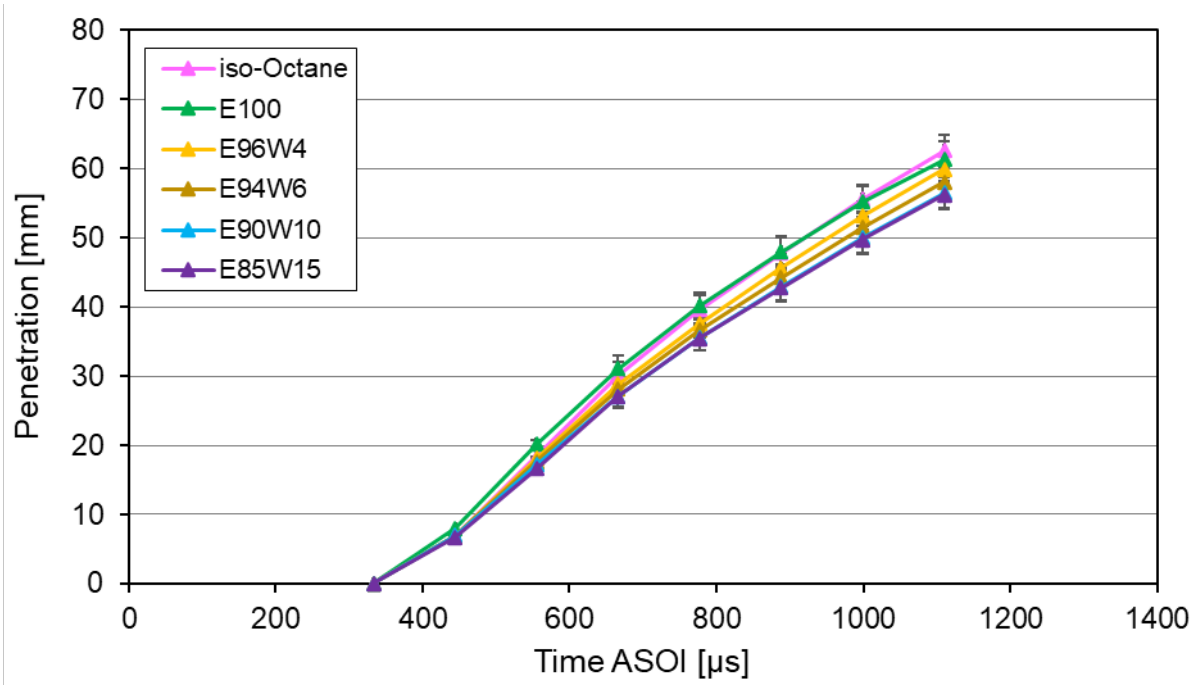

Figure 22. Side view spray plume pair A penetration: 20 °C, 1.0 bar.

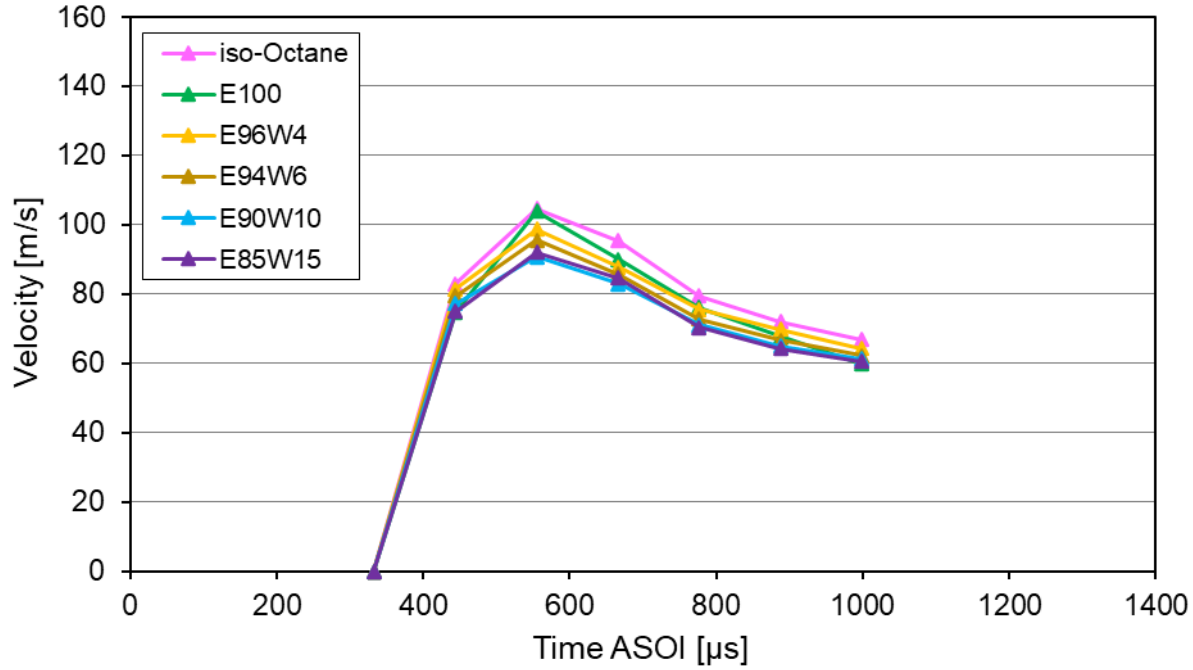

Figure 23. Side view spray plume pair A velocity: 20 °C, 1.0 bar.

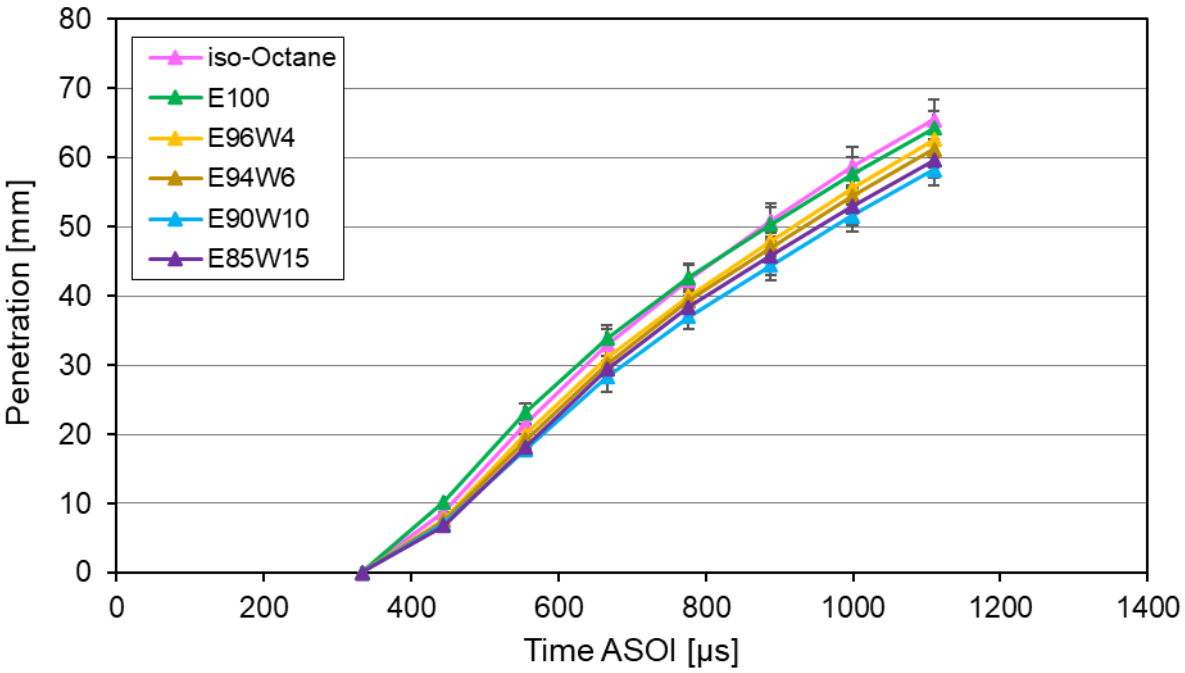

Figure 24. Side view spray plume pair A penetration: 20 °C, 0.5 bar.

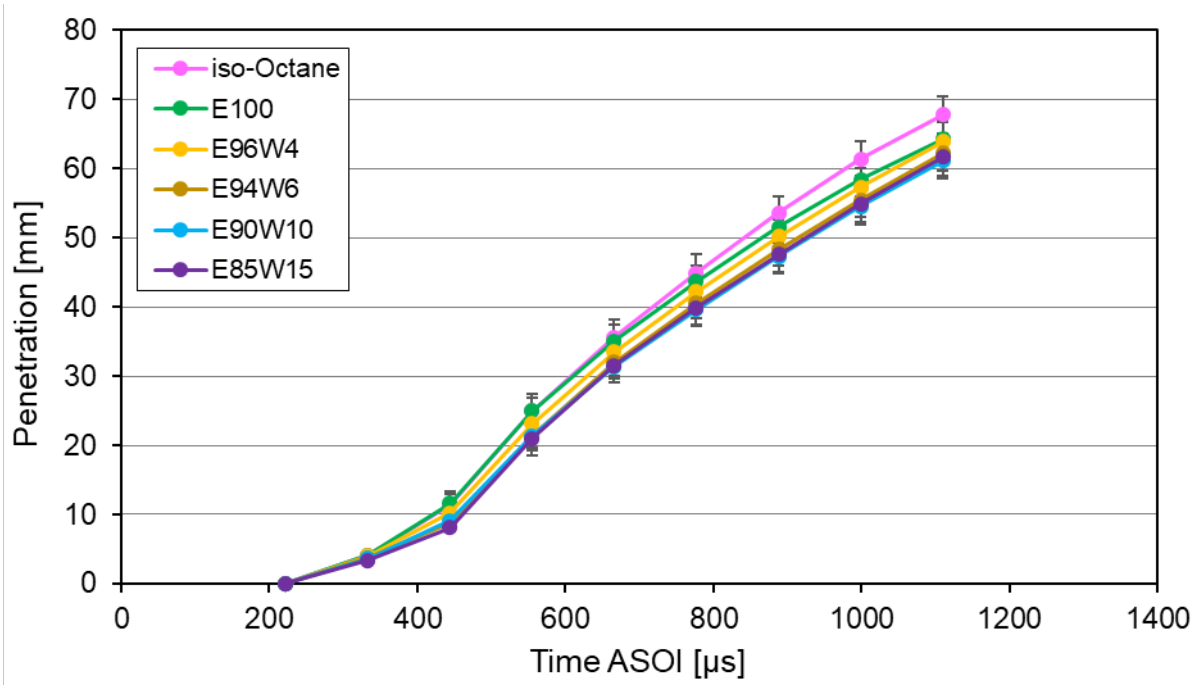

Figure 25. Side view spray plume pair A penetration: 50 °C, 0.5 bar.

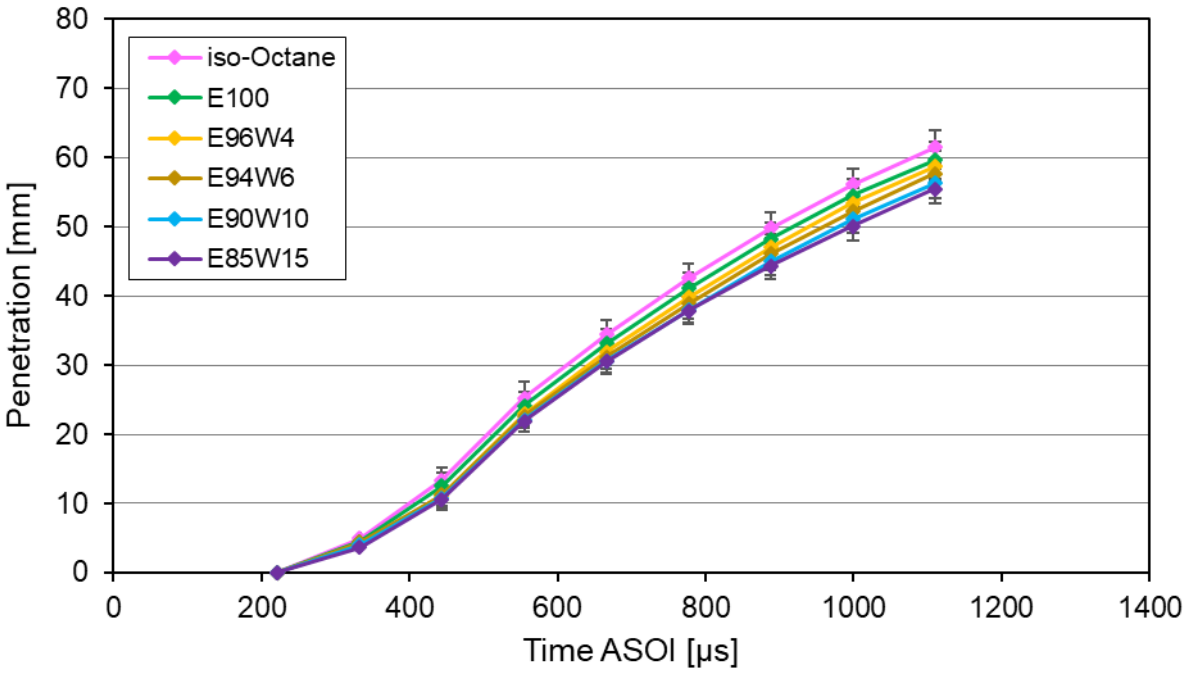

Figure 26. Side view spray plume pair A penetration: 90 °C, 1.0 bar.

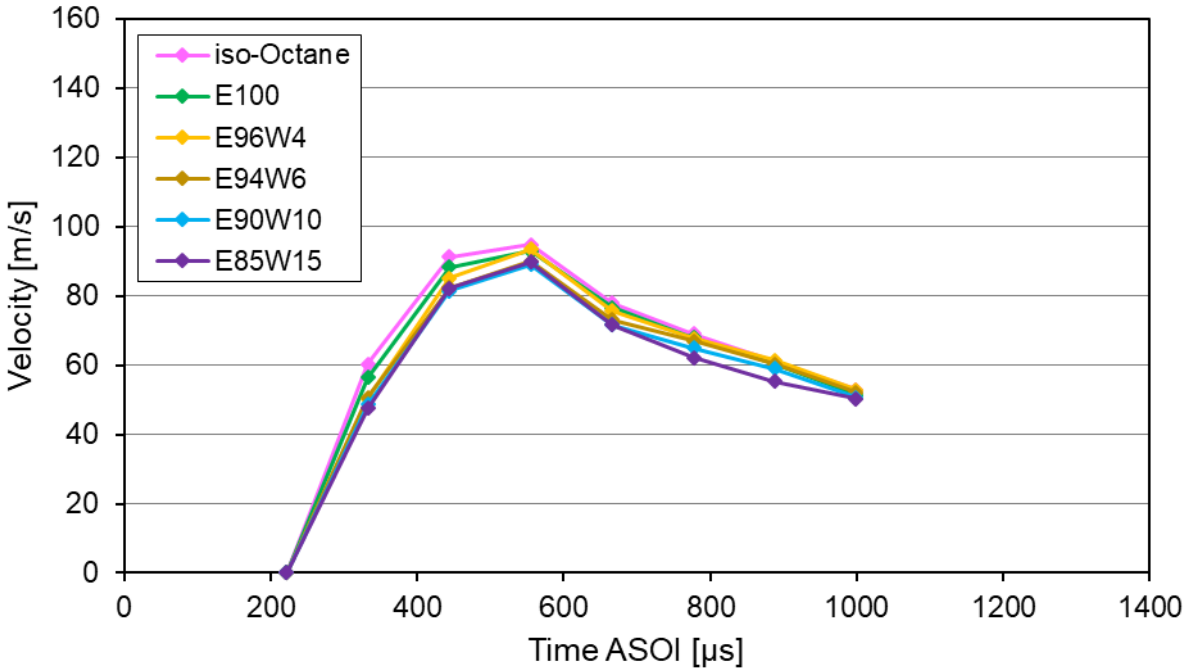

Figure 27. Side view spray plume pair A velocity: 90 °C, 1.0 bar.

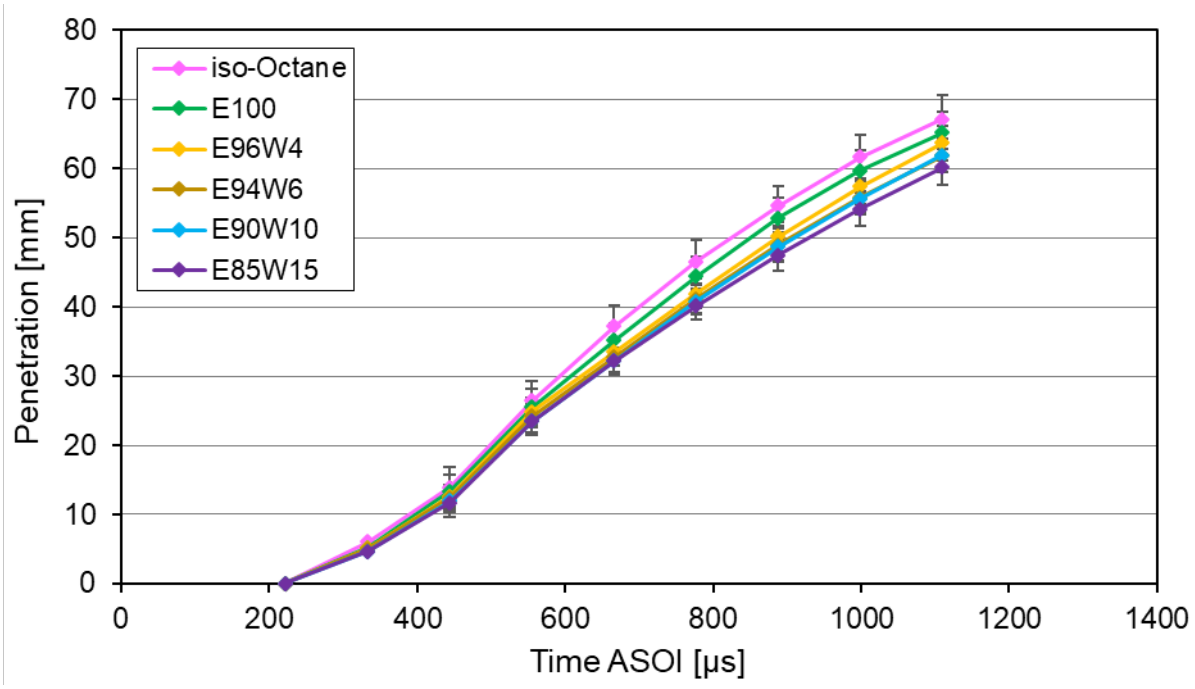

Figure 28. Side view spray plume pair A penetration: 90 °C, 0.5 bar.

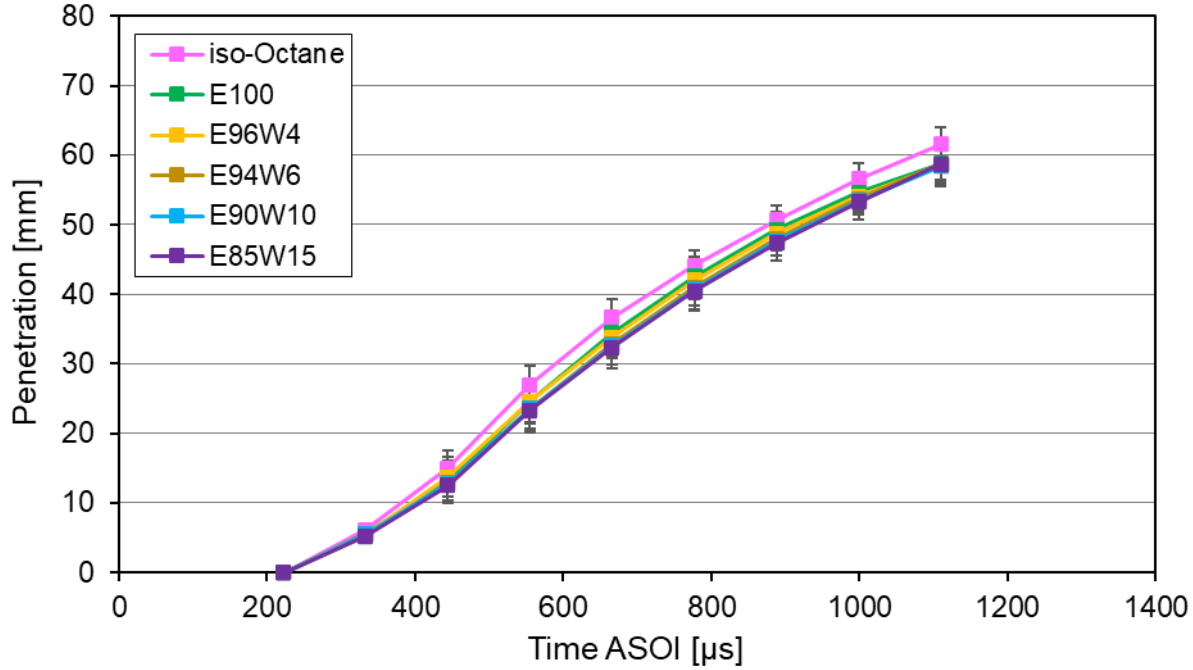

Figure 29. Side view spray plume pair A penetration: 110 °C, 1.0 bar.

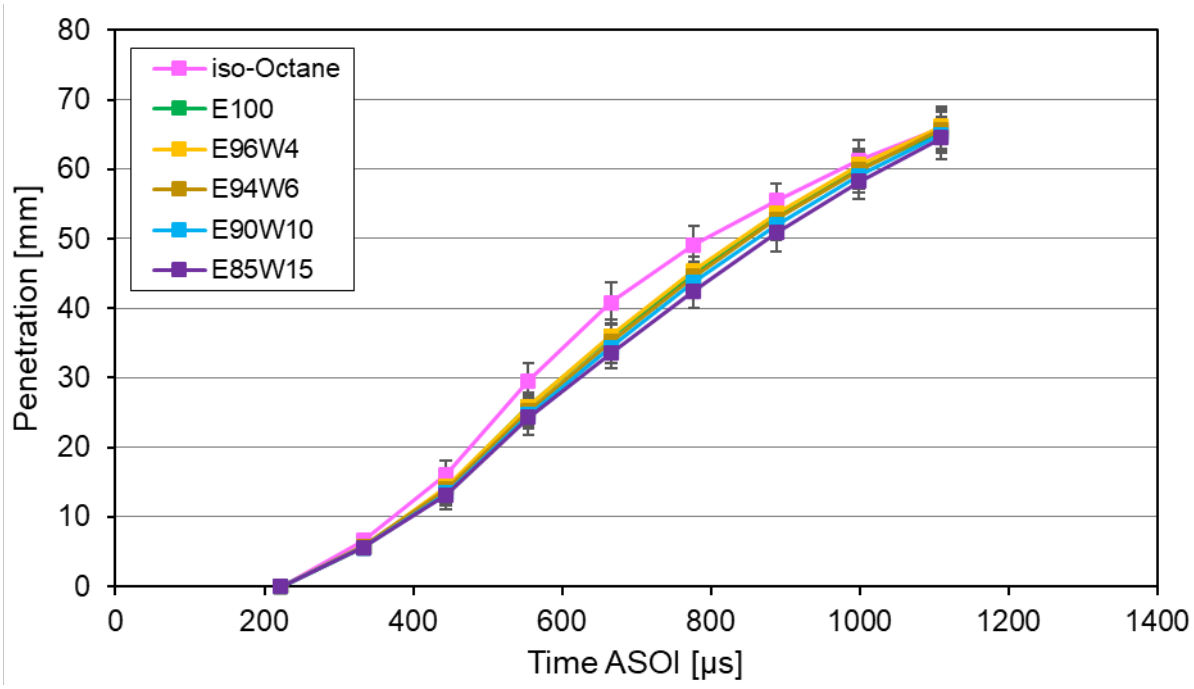

Figure 30. Side view spray plume pair A penetration: 110 °C, 0.5 bar.

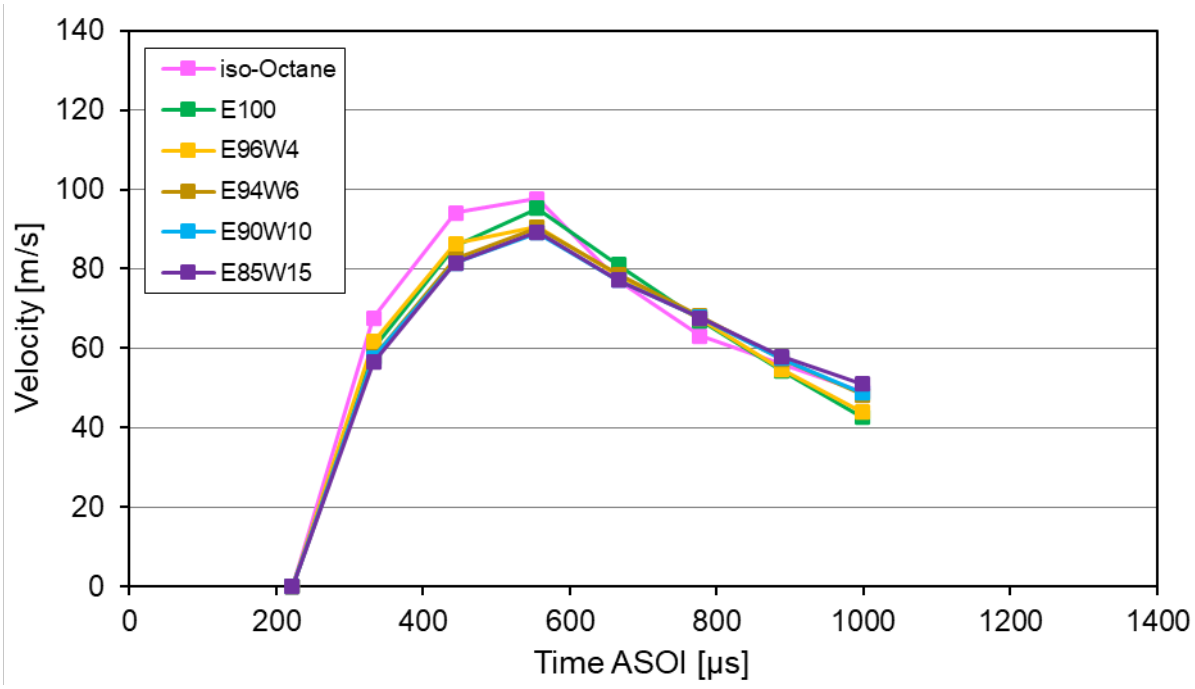

Figure 31. Side view spray plume pair A velocity: 110 °C, 1.0 bar.

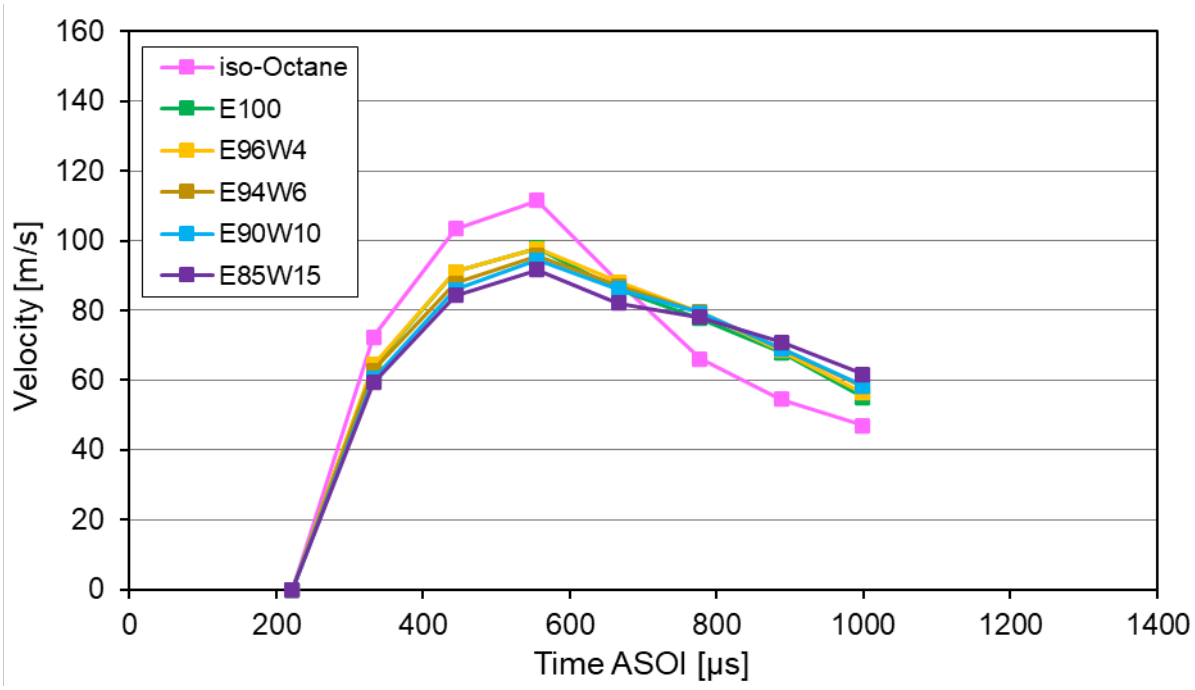

Figure 32. Side view spray plume pair A velocity: 110 °C, 0.5 bar.

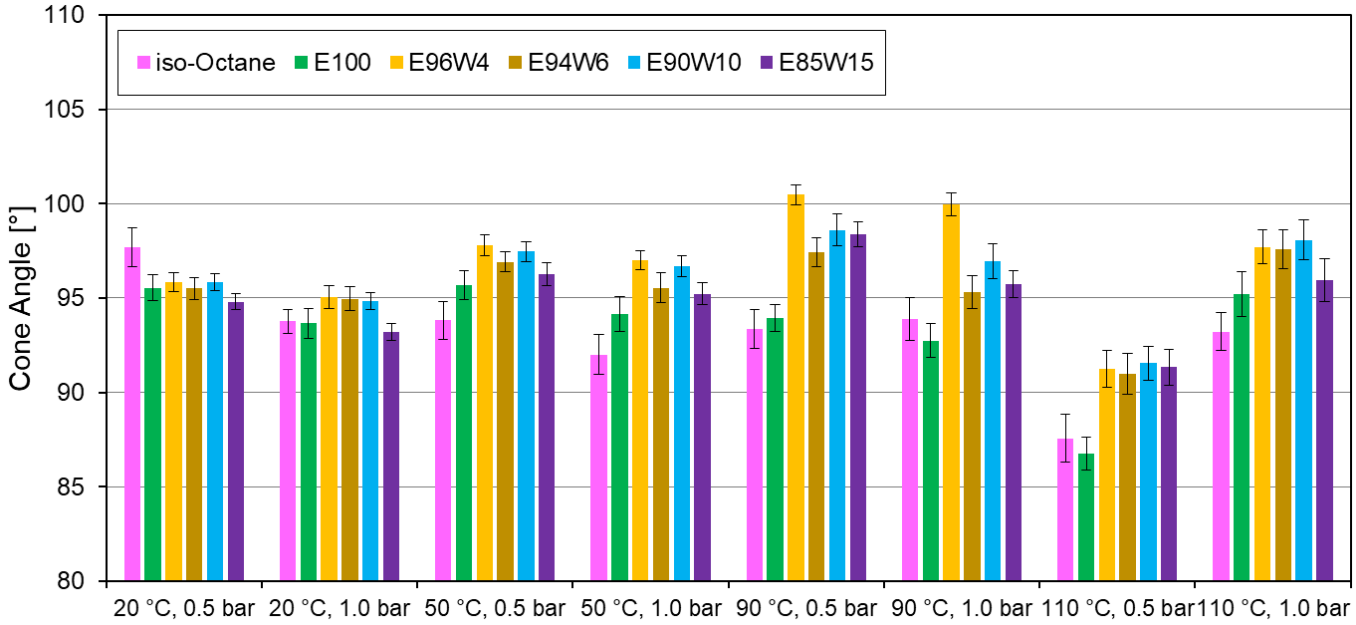

Figure 33. Side view combined cone angle for all plumes.

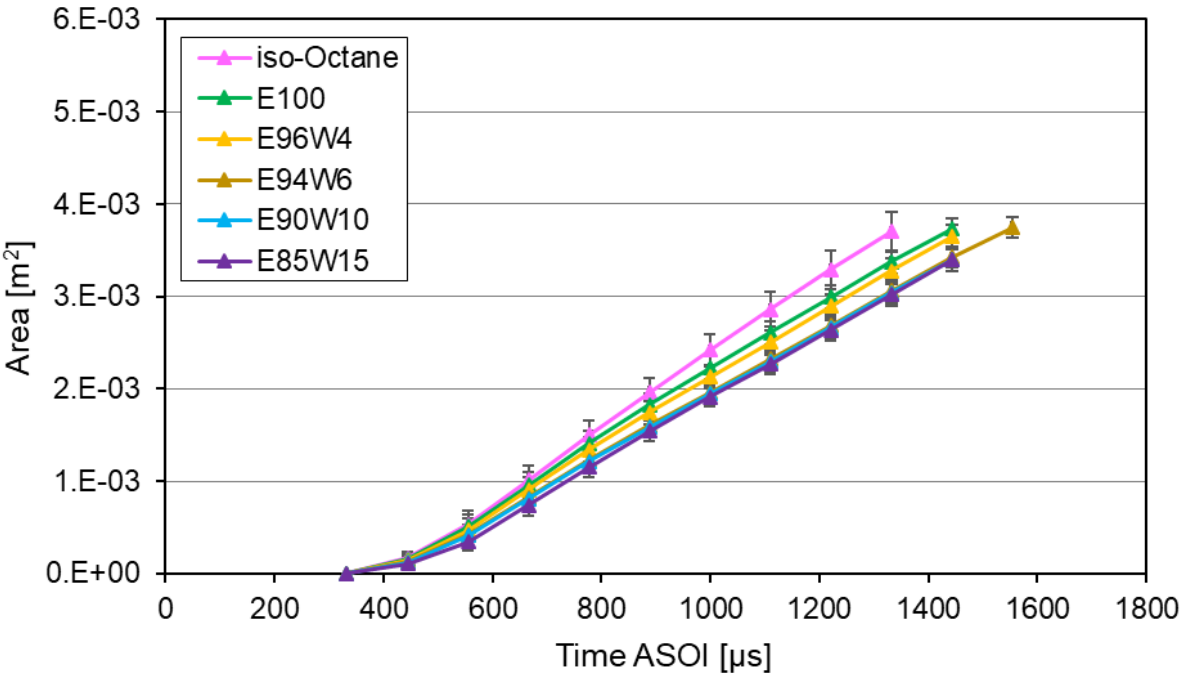

Figure 34. Base view spray area at 20 °C, 1.0 bar.

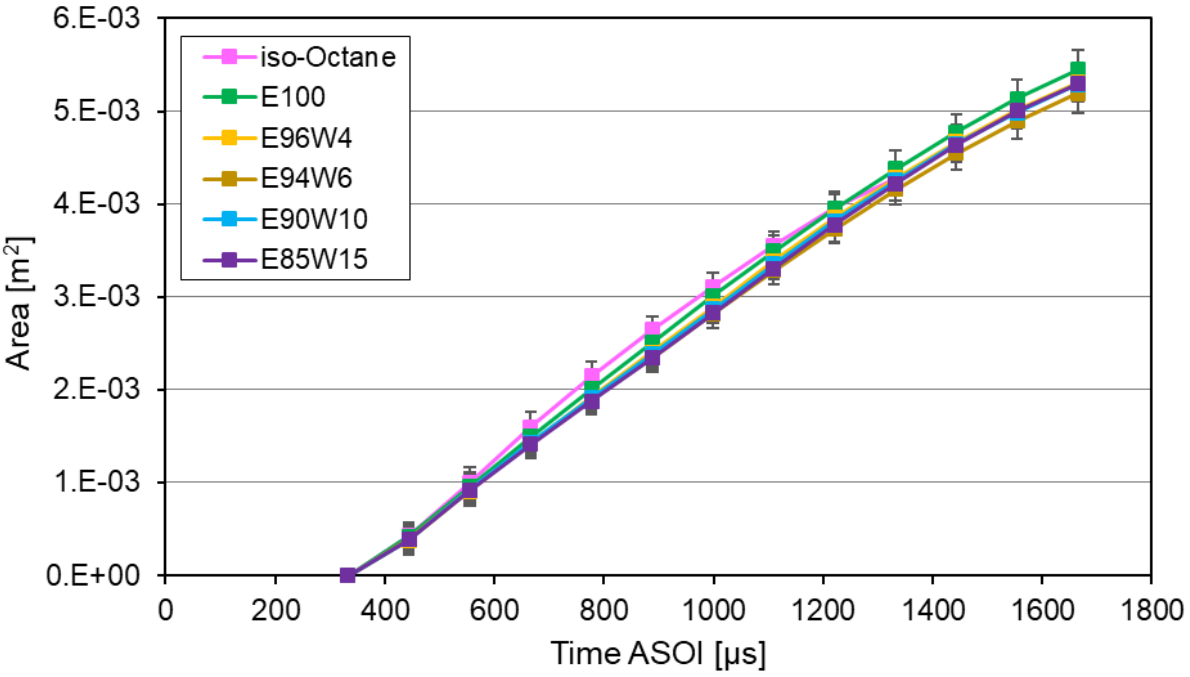

Figure 35. Base view spray area at 110 °C, 0.5 bar.

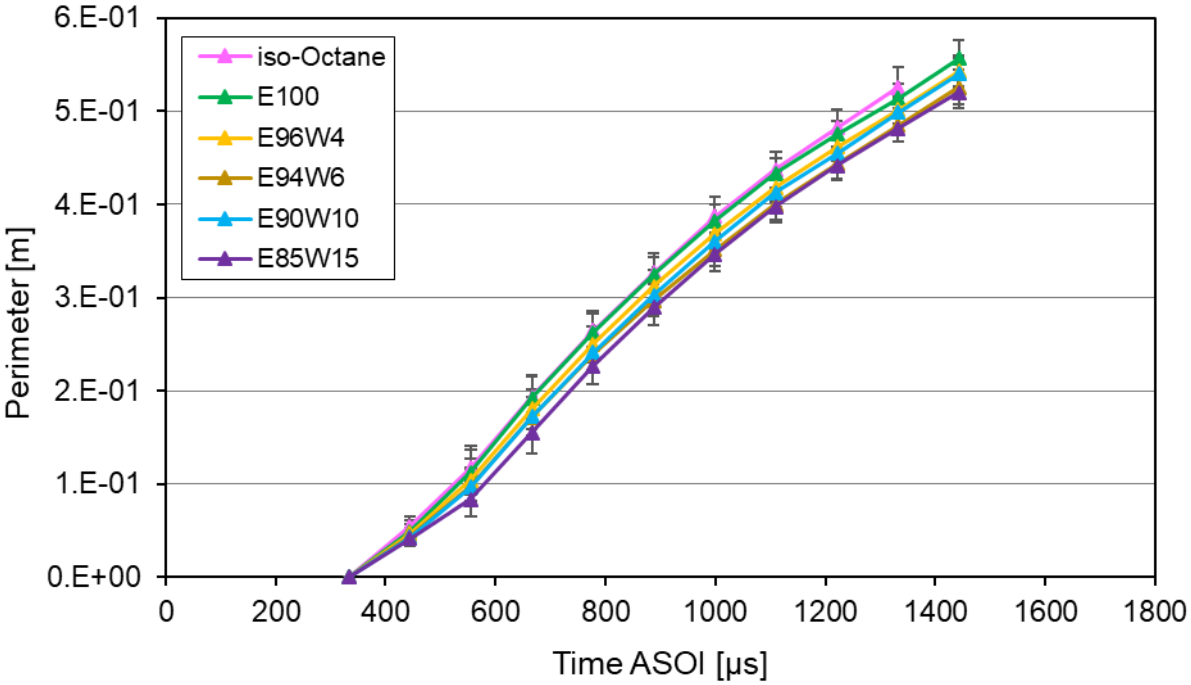

Figure 36. Base view spray perimeter at 20 °C, 1.0 bar.

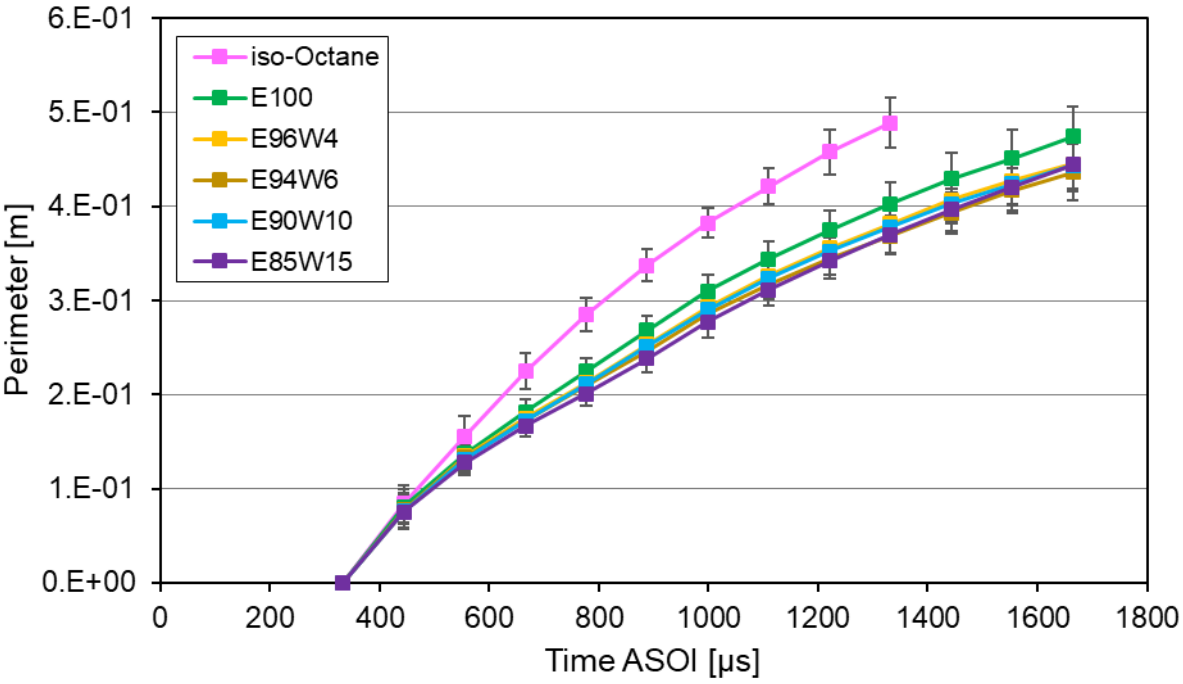

Figure 37. Base view spray perimeter at 110 °C, 0.5 bar.

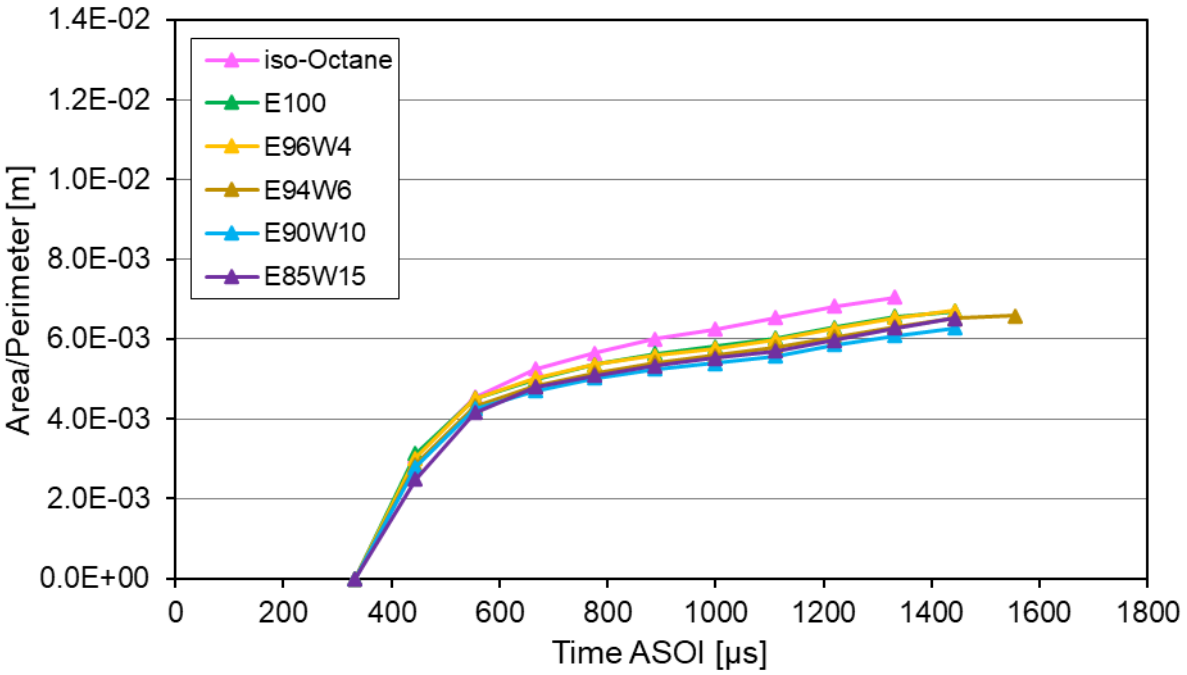

Figure 38. Base view spray area/perimeter ratio at 20 °C, 1.0 bar.

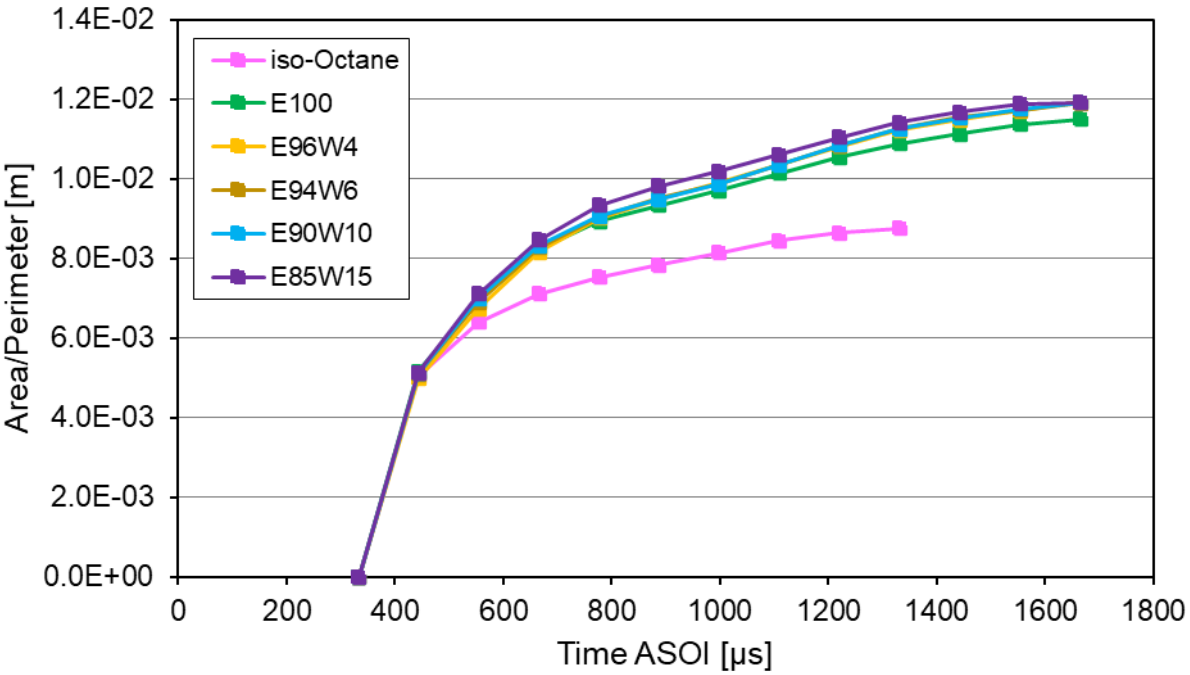

Figure 39. Base view spray area/perimeter ratio at 110 °C, 0.5 bar.

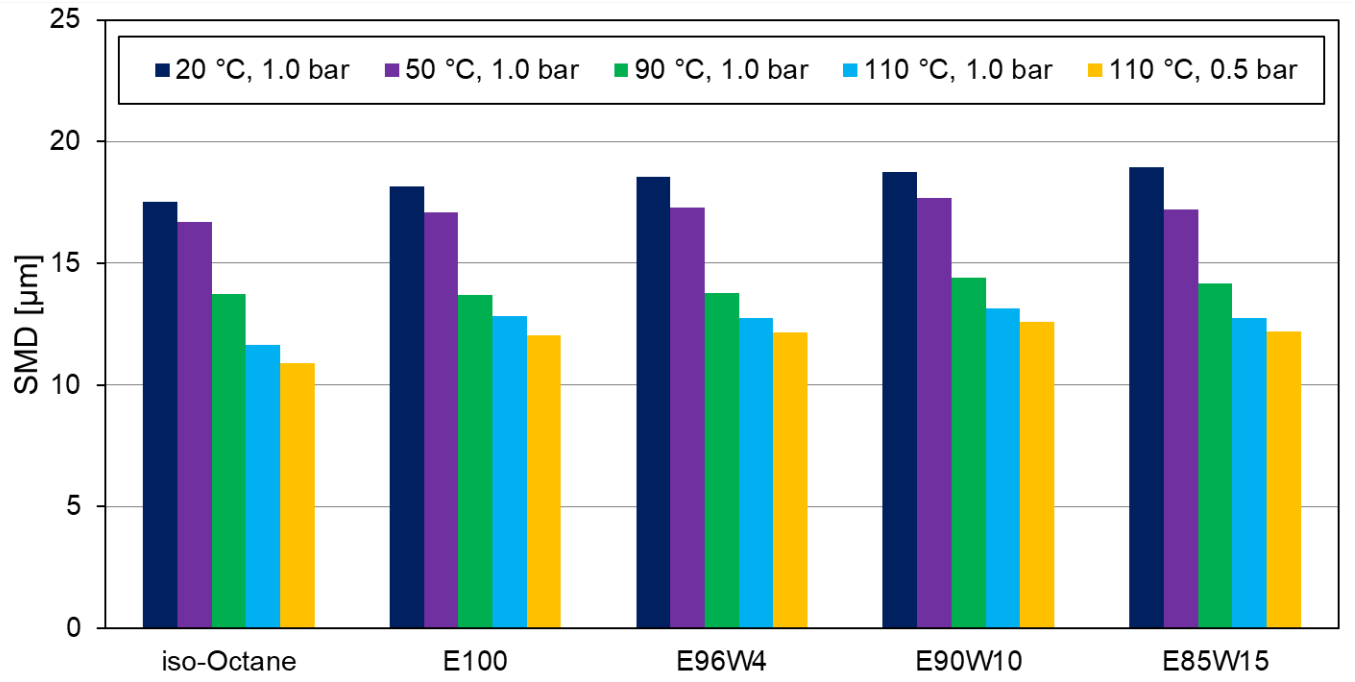

Figure 40. SMD at various temperatures and pressures, all fuels.

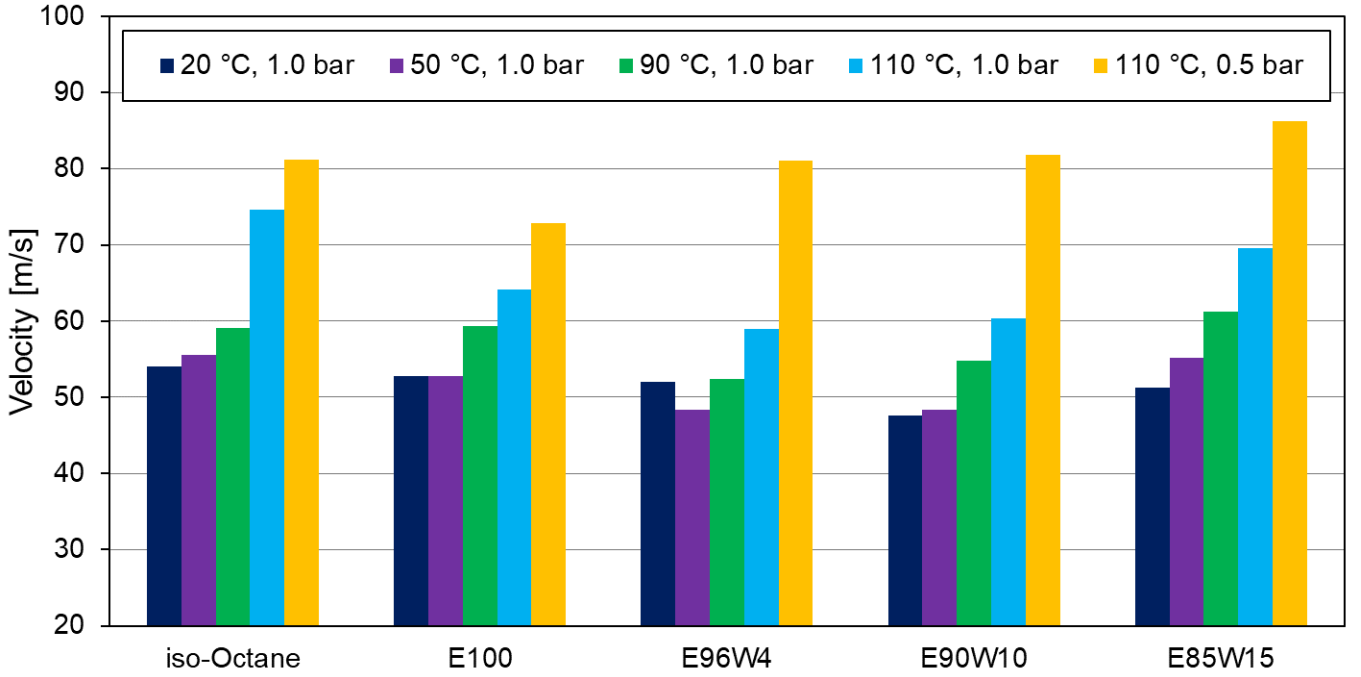

Figure 41. Mean droplet velocity at various temperatures and pressures, all fuels.